

Electrically Tunable Interband Collective Excitations in Biased Bilayer and Trilayer Graphene

Tomer Eini,¹ M. F. C. Martins Quintela,^{2,3,4,5,6} J. C. G. Henriques,^{3,7} R. M. Ribeiro,^{3,8} Yarden Mazor,¹ N. M. R. Peres,^{3,8,9} and Itai Epstein^{1,10,11,*}

¹*School of Electrical Engineering, Faculty of Engineering, Tel Aviv University, Tel Aviv 6997801, Israel*

²*Department of Physics and Physics Center of Minho and Porto Universities (CF-UM-UP), Campus of Gualtar, 4710-057, Braga, Portugal*

³*International Iberian Nanotechnology Laboratory (INL), Av. Mestre José Veiga, 4715-330, Braga, Portugal*

⁴*Department of Materials and Production, Aalborg University, 9220 Aalborg Øst, Denmark*

⁵*Departamento de Química, Universidad Autónoma de Madrid, 28049 Madrid, Spain*

⁶*Condensed Matter Physics Center (IFIMAC), Universidad Autónoma de Madrid, 28049, Madrid, Spain*

⁷*Universidade de Santiago de Compostela, 15782 Santiago de Compostela, Spain*

⁸*Centro de Física das Universidades do Minho e do Porto (CF-UM-UP) e Departamento de Física, Universidade do Minho, P-4710-057 Braga, Portugal*

⁹*POLIMA—Center for Polariton-driven Light-Matter Interactions,*

University of Southern Denmark, Campusvej 55, DK-5230 Odense M, Denmark

¹⁰*Center for Light-Matter Interaction, Tel Aviv University, Tel Aviv 6997801, Israel*

¹¹*QuanTAU, Quantum Science and Technology Center, Tel Aviv University, Tel Aviv 6997801, Israel*

(Dated: December 2024)

Collective excitations of charged particles under the influence of an electromagnetic field give rise to a rich variety of hybrid light-matter quasiparticles with unique properties. In metals, intraband collective response manifested by negative permittivity leads to plasmon-polaritons with extreme field confinement, wavelength "squeezing", and potentially low propagation losses. In contrast, photons in semiconductors commonly couple to interband collective response in the form of exciton-polaritons, which give rise to completely different polaritonic properties, described by a superposition of the photon and exciton and an anti-crossing of the eigenstates. In this work, we identify the existence of plasmon-like collective excitations originating from the interband excitonic response of biased bilayer and trilayer graphene, in the form of graphene-exciton-polaritons (GEPs). We find that GEPs possess electrically tunable polaritonic properties and discover that such excitations follow a universal dispersion law for all surface polaritons in 2D excitonic systems. Accounting for nonlocal corrections to the excitonic response, we find that the GEPs exhibit confinement factors that can exceed those of graphene plasmons, and with moderate losses that would enable their observation in cryo-SNOM experiments. Furthermore, by electrically tuning the excitons' energy into the Reststrahlen band of the surrounding hexagonal-boron-nitride, we demonstrate that strong coupling between the excitons and hyperbolic phonon polaritons can be achieved, and well-described by an electromagnetic transmission line model. These predictions of plasmon-like interband collective excitations in biased graphene systems open up new research avenues for tunable plasmonic phenomena based on excitonic systems, and the ability to control and manipulate such phenomena at the atomic scale.

I. INTRODUCTION

Collective excitation can be described as the interaction between dipole oscillations of charged (quasi-) particles and the electromagnetic field oscillations of an impinging photon. Fundamentally, this interaction forms a new quasi-particle, i.e. the polariton, which inherits its properties from both the photon and the material excitation, constituting an eigenmode of the overall electromagnetic field in the system. The vast variety of such interacting quasi-particles give rise to numerous types of polaritons, such as plasmon-polaritons, exciton-polaritons, phonon-polaritons, hyperbolic-polaritons, cooper pair polaritons, magnon-polaritons, and more [1–9].

Different types of polaritons can be further classified to families with similar properties. For example, surface polaritons that propagate in the in-plane direction of an interface between two materials, where one of the materials exhibits a negative real part of its permittivity, are characterized as highly confined optical modes due to their ability to carry large momentum in the propagation direction. Surface polaritons can thus be supported in any material exhibiting negative permittivity, e.g. surface-plasmon-polaritons in metals [10–13], surface-exciton-polaritons in semiconductors [14–18], graphene plasmons [4, 5, 19–21], surface and hyperbolic phonon-polaritons in polar dielectric [6–8, 22, 23], and more.

Another important polaritonic family is that described by the phenomena of strong coupling between two states, which results in the superposition, or hybridization, of the states into two new eigenmodes that are char-

* itaieps@tauex.tau.ac.il

acterized by a Rabi splitting and its resulting anti-crossing [9, 24–29]. Although the interacting states can be quantum, classical analogs have been developed to describe such strong and weak coupling regimes [30]. Exciton-polaritons formed by a semiconductor exciton interacting with a cavity photon are an exemplary system for such strong coupling, resulting in hybridized exciton-polaritons and the possible demonstration of Bose–Einstein condensates [26, 31].

In the last decade, two-dimensional (2D) materials have drawn significant interest as a versatile platform for studying polaritons at the atomic scale [1–3, 7]. The unique properties of these materials, such as their low dimensionality, pronounced quantum effects, and natural anisotropy, give rise to quasi-particles that strongly interact with light, which can be readily controlled via their surrounding, charged carrier density, and temperature [19, 20, 32–35]. Moreover, they can be easily integrated into van der Waals heterostructures and cavities yielding enhanced response and hybridization [9, 29, 36–40].

Recently, several graphene-based material systems have been demonstrated to exhibit unique excitonic response, such as Bernal-stacked and twisted Bilayer Graphene (BLG), and Rhombohedral Trilayer Graphene (RTG) [41–46]. In their native form, the BLG and RTG are semi-metallic with a zero bandgap and a non-conical band structure. However, when encapsulated in an isolating material, such as hexagonal-boron-nitride (hBN), inversion symmetry can be broken by applying a bias that forms an electric field across the graphene layers. This results in the opening of a bandgap and the system thus becomes semiconducting [47–49], with the ability to support excitons with large binding energies [41–45], similar to excitons in 2D semiconductors [50].

In this work, we unveil the existence of plasmon-like collective excitations, typically associated with intraband responses, within the interband excitonic regime of biased BLG and RTG (BBLG and BRTG), in the form of graphene-exciton-polaritons (GEPs). We find that GEPs possess electrically tunable polaritonic properties at far-infrared (FIR) frequencies, and we discover that such interband excitation follow a universal dispersion law for all surface polaritons in 2D excitonic systems. Taking into account the appropriate nonlocal corrections, we analytically derive the dispersion relations of the GEPs and study their electrically tunable polaritonic properties: confinement, loss, and field distribution. We find that GEPs can reach confinement factors that are larger than those of graphene plasmons, and with moderate losses that would enable their observation in cryo-SNOM experiments. Furthermore, we show that the GEPs’ properties can be electrically controlled and spectrally tuned through the biasing of the BBLG and BRTG systems. By tuning the excitons spectrally into the hBN’s Reststrahlen band, we find multiple strongly coupled hybridized states of excitons and hyperbolic-phonon-polaritons (HPhPs) in the FIR spec-

trum. We derive the dispersion relations of these hybridized states using a electromagnetic transmission line model and show that they are highly affected and manipulated by the symmetry of the system.

II. OPTICAL EXCITONIC CONDUCTIVITY OF BBLG AND BRTG

The systems under investigation in this work are the BBLG and the BRTG, each separately encapsulated by hBN (Fig. 1). The gap is opened by an applied bias between two electrodes placed above and below the encapsulating hBN, forming a dual-gated metal-oxide-semiconductor-field-effect-transistor (MOS-FET), with the electric field across the graphene system being electrically controlled by the bias [41–45].

Under these conditions, the optical response of the BBLG and BRTG systems is given by the inclusion of the excitonic response into their optical conductivities,

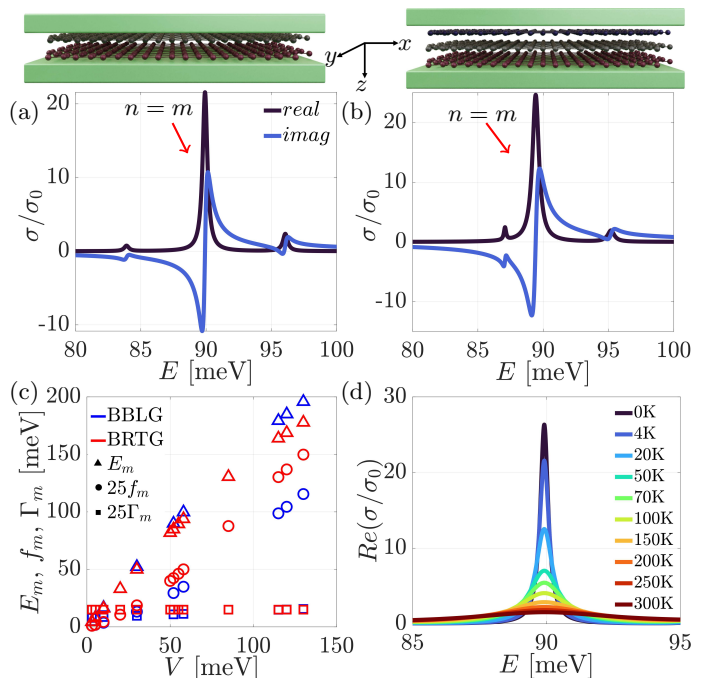


FIG. 1. Optical conductivity of (a) BBLG for $V = 52$ meV, and (b) BRTG for $V = 55$ meV, obtained from Eq. 1, both for $T = 4K$. Both the BBLG and BRTG exhibit positive values of the imaginary part of the conductivity, due to the excitonic resonances. The main resonances $n = m$ are marked with arrows. The configurations of BBLG and BRTG encapsulated by hBN are illustrated above the figure. (c) Voltage dependence of the exciton energy, oscillator strength and non-radiative decay rate of the main resonance of BBLG (blue) and BRTG (red) for $T = 4K$. (d) Temperature dependence of the real part of the conductivity of BBLG for $V = 52$ meV.

taking the form [41, 42]:

$$\sigma = 4i\sigma_0 \sum_n \frac{f_n}{E - E_n + i\frac{\Gamma_n}{2}}, \quad (1)$$

where $\sigma_0 = \frac{e^2}{4h}$ is the universal conductivity of graphene, E is the energy, f_n , E_n and Γ_n are the oscillator strength, exciton energy, and non-radiative decay rate of the excitonic resonance of the n th exciton Rydberg series. This optical conductivity is obtained directly from the dynamical equation of the density matrix when considering a perturbation by a monochromatic field, taking into account the effect of the applied bias [41, 42, 51–55] (see appendix A). From now on we will focus on the main resonance $n = m$, with the largest oscillator strength, as it dominates the optical response (Fig. 1 (a) and (b)).

The conductivities of BBLG and BRTG from Eq. 1 are presented in Fig. 1 (a) and (b), respectively. It can be seen that in both cases, positive values of the imaginary part of σ can be observed, stemming from the excitonic resonances of the biased graphene systems, as will be discussed further in section III. In addition, we note that these conductivities depend on the bias voltage [41, 42] and temperature [56], affecting the oscillator strength and the non-radiative decay rate (Fig. 1 (c) and (d)) (see Appendices B and C). In Fig. 1 (d), the affect of temperature on the BBLG conductivity can be seen, resulting in the broadening of the excitonic resonance due to interaction with phonons. The exact temperature dependence of the BRTG conductivity could not be similarly calculated, owing to the lack of information in the literature on the parameters required for the phonon-exciton scattering computation (appendix C). Thus, following [42] we take the BRTG linewidth to be constant.

III. GRAPHENE-EXCITON-POLARITON

The basis of the existence of surface polaritons and their unique properties stems from materials possessing negative real part of their permittivity (positive values of the imaginary part of their conductivity) [6, 10, 56–59]. Therefore, the positive imaginary values exhibited by the BBLG and BRTG conductivities (Fig 1 (a) and (b)) imply that these systems support surface polaritons. Since it is the excitonic contribution to the conductivity of the graphene systems that provides these positive values in the imaginary part, and thus its polaritonic response, we refer to these as Graphene-Exciton-Polaritons (GEPs).

The dispersion relation of the GEPs in these structures is described by (appendix F):

$$q_{GEP} = \frac{2i\varepsilon_0\varepsilon_{hBN_{eff}}\omega}{\sigma}, \quad (2)$$

where q_{GEP} is the component of the wavevector in the x direction (the momentum), ω is the angular frequency, $\varepsilon_{hBN_{xx}}$, $\varepsilon_{hBN_{zz}}$ and $\varepsilon_{hBN_{eff}} = \sqrt{\varepsilon_{hBN_{xx}}\varepsilon_{hBN_{zz}}}$ are the

in-plane x , out-of-plane z and effective permittivity of hBN [60], and σ is the conductivity of either BBLG or BRTG (Eq. 1).

The general properties of the GEPs can now be assessed by evaluating the confinement factor, $\lambda_0/\lambda_{GEP} = Re(q_{GEP})/k_0$, and the loss figure described by inverse damping ratio $\gamma_p^{-1} = Re(q_{GEP})/Im(q_{GEP})$ [7, 35, 60], where $\lambda_0 = \frac{2\pi}{k_0}$ is the free-space wavelength, $k_0 = \frac{\omega}{c}$ is the free-space wavenumber, c is the speed of light in vacuum, and $\lambda_{GEP} = \frac{2\pi}{Re(q_{GEP})}$ is the GEP wavelength. Figure 2 (a) and (c) show the confinement factor and inverse damping ratio of BBLG GEPs, respectively, for the optimal voltage $V = 52$ meV and temperature $T = 4$ K, i.e., the largest confinement factors with minimal propagation losses. Excellent agreement between the transfer matrix method (TMM) simulation (colormap) and the analytical solution obtained from Eq. 2 (dashed red line) can be seen. Similarly, Fig. 2 (b) and (d) show the confinement factor and inverse damping ra-

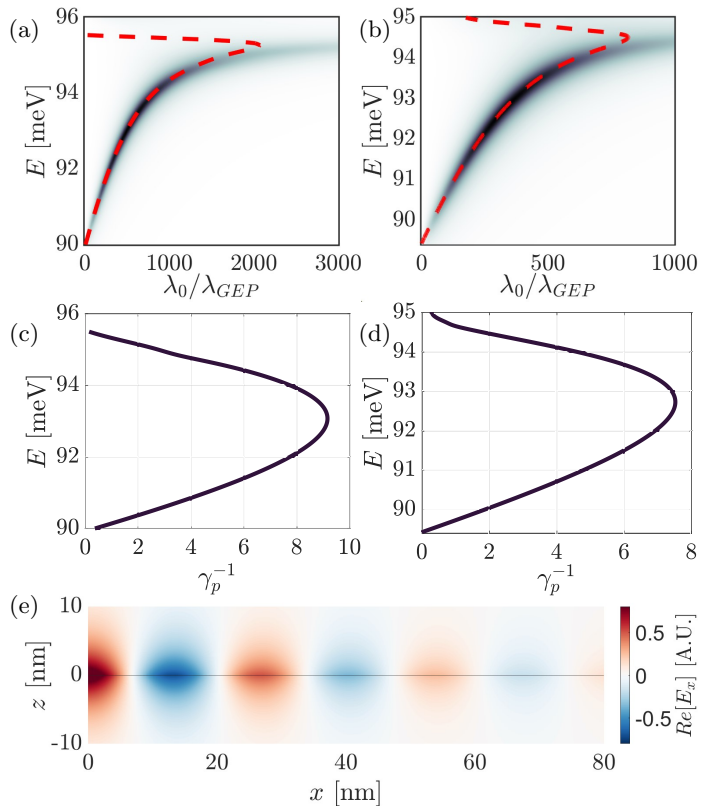


FIG. 2. Polaritonic properties of GEP. Confinement factor of GEP λ_0/λ_{GEP} , for BBLG for $V = 52$ meV (a) and for BRTG for $V = 55$ meV (b), both for $T = 4$ K, calculated from Eq. 2 (dashed red line) and simulated using a TMM (colormap). The confinement reaches two and three orders of magnitude. Inverse damping ratio of GEP $\gamma_p^{-1} = Re(q_{GEP})/Im(q_{GEP})$, for BBLG (c) and BRTG (d). (e) The electromagnetic field distribution of GEP in BBLG at $E = 93$ meV, the graphene is marked at $z = 0$. The polaritons propagate with losses in the in-plane direction and decay in the out-of-plane direction.

tio of BRTG GEPs, respectively, for the optimal voltage $V = 55$ meV for BRTG, and temperature $T = 4$ K. It can be seen from Fig. 2 (a) and (b) that the GEPs in both systems are extremely confined, showing up to two orders of magnitude factors for the BRTG and even three orders of magnitude for the BBLG. These confinement factors are much larger than those observed for graphene plasmons [32, 61–64]. However, we note that these confinement factors are accompanied by propagation lengths over ten times smaller than those of graphene plasmons at low temperatures [35]. In addition, the results obtained in Fig. 2 are based on the local description of the optical response, which only applies for low momentum modes. For the appropriate description of high momentum modes, one must take into account the nonlocal, momentum-dependent response, which will alter both the confinement factor and propagation losses of the graphene systems, as will be addressed in section IV. For completeness, Fig. 2 (e) show the electric field distribution of the BBLG GEPs (appendix F).

Intuitively, we can obtain simpler expressions for the confinement factor and inverse damping ratio by examining the conductivity near this main resonance, where $|E - E_n| \gg \Gamma_n$ for $n \neq m$ and $|E - E_m| \lesssim \Gamma_m$, and thus the contribution of the additional resonances is negligible. We can therefore approximate the conductivity as:

$$\sigma \approx \frac{4i\sigma_0 f_m}{E - E_m + i\frac{\Gamma_m}{2}}. \quad (3)$$

By inserting Eq. 3 into Eq. 2 we obtain the approximated expression for the dispersion relation:

$$q_{GEP} = \frac{\varepsilon_0 \varepsilon_{hBN_{eff}} \omega}{2\sigma_0 f_m} \left(E - E_m + i\frac{\Gamma_m}{2} \right). \quad (4)$$

Then the confinement factor and inverse damping ratio can be approximately expressed by (appendix F):

$$\lambda_0 / \lambda_{GEP} = \frac{\varepsilon_0 \varepsilon_{hBN_{eff}} c}{2\sigma_0 f_m} (E - E_m), \quad (5)$$

$$\gamma_p^{-1} = 2 \frac{E - E_m}{\Gamma_m}. \quad (6)$$

In addition, by neglecting losses, the dispersion relation in Eq. 4 can be expressed in terms of $\omega(q_{GEP})$:

$$\omega = \frac{\omega_m}{2} + \sqrt{\frac{2\sigma_0 f_m}{\varepsilon_0 \varepsilon_{hBN_{eff}} \hbar} q_{GEP} + \left(\frac{\omega_m}{2} \right)^2}, \quad (7)$$

where $\omega_m = \frac{E_m}{\hbar}$ is the angular frequency of the exciton resonance. Despite the fundamental plasmonic nature of the GEPs, as they are based on the existence of positive

values of the imaginary part of the conductivity, Eq. 7 differs significantly from the commonly known dispersion relation expected in all two-dimensional electronic systems [65]. This behavior stems directly from the unique excitonic nature of these plasmon-like polaritons in comparison to plasmons in electronic systems. A clear shift in the exciton energy and momentum can be seen in the dispersion relation, introducing a new universal relation for surface polaritons in 2D excitonic systems.

We note that the polaritonic properties of the GEPs can be similarly evaluated for every bias voltage and every temperature for which the BBLG or BRTG presents positive values of the imaginary part of the conductivity. It can be seen from Fig. 1 (c) that the oscillator strength increases with bias voltage, suggesting that larger confinement factors can be obtained for lower voltages (Eq. 5). However, the effective permittivity of hBN, which also affects the confinement factor via Eq. 5, is frequency dependent, as will be further discussed in section V, and its real part obtains maximum values below and close to the hBN's Reststrahlen bands [6]. By examining the dependence of Eq. 5 on the voltage, we find that the largest confinement is obtained for a bias voltage of $V = 52$ meV for BBLG and of $V = 55$ meV for BRTG, which correspond to an exciton energy of $E_m \approx 90$ meV, just below the lower Reststrahlen band of hBN (Fig. 4 (a)). From Eq. 6, we get that the inverse damping ratio increases with decreasing temperature due to a reduction in exciton-phonon interaction. Since $T = 0$ K is a theoretical limit we choose $T = 4$ K as the optimal temperature.

IV. NONLOCAL EFFECTS

Next, we introduce the nonlocal correction to enhance the robustness and accuracy of our theoretical framework. Nonlocal effects describe the interaction between excitations in the material that cause the current at point \mathbf{r} to depend on the value of the field at another point $\mathbf{r}' \neq \mathbf{r}$. In the momentum space, this leads to an optical response of the material that depends on the momentum as well as energy. In semiconductors, nonlocal effects are a result of coupling between neighboring excitons [57, 66, 67] and leads to a shift of the exciton energy described by the term $\frac{\hbar^2 q^2}{2m_X}$, where m_X is the exciton's effective mass. This approach holds for $\frac{\hbar^2 q^2}{2m_X} \ll E_m$, such that the correction to the exciton energy is small. To examine the conductivity near the main resonance where Eq. 3 holds, we neglect again the contribution of the additional resonances by assuming $|E - E_n| \gg \Gamma_n$ for $n \neq m$ and $|E - E_m| \lesssim \Gamma_m$. Thus, we obtain the expression for the nonlocal conductivity by setting $E_m \rightarrow E_m + \frac{\hbar^2 q^2}{2m_X}$ in Eq. 3:

$$\sigma = \frac{4i\sigma_0 f_m}{E - (E_m + \frac{\hbar^2 q^2}{2m_X}) + i\frac{\Gamma_m}{2}}, \quad (8)$$

with m_X in the BBLG given by (appendix L):

$$m_X = \frac{\gamma_1(4V^2 + \gamma_1^2)^{\frac{3}{2}}}{16Vv_f^2(2V^2 + \gamma_1^2)}, \quad (9)$$

where $v_f = \frac{3a\gamma_0}{2\hbar}$ is the Fermi velocity, $a = 2.46 \text{ \AA}$ is the lattice constant of graphene, $\gamma_0 = 3 \text{ eV}$ and $\gamma_1 = 0.4 \text{ eV}$ are the nearest neighbors intralayer and interlayer hoppings. The exciton's effective mass of BRTG is calculated in the same approach as in appendix L, but numerically

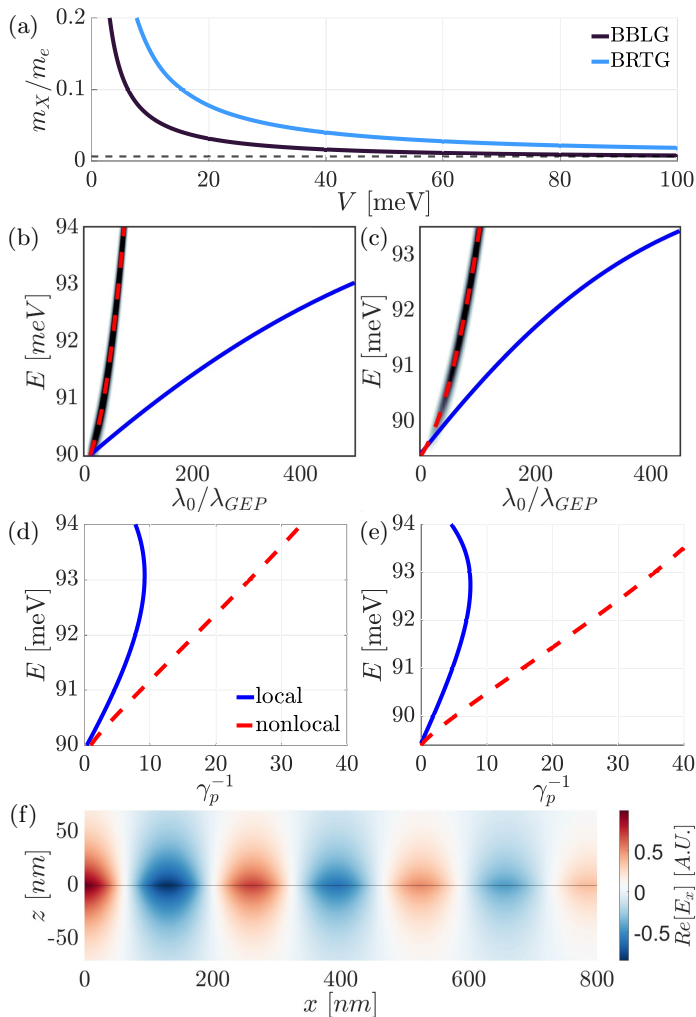


FIG. 3. Nonlocal corrections. (a) Voltage dependence of the exciton's effective mass, calculated from Eq. 9 for BBLG and numerically for BRTG, normalized by the electron mass. Confinement factor of GEP λ_0/λ_{GEP} , for BBLG for $V = 52 \text{ meV}$ (b) and for BRTG for $V = 55 \text{ meV}$ (c), both for $T = 4 \text{ K}$, including nonlocal effects, calculated from Eq. 11 (dashed red line) and simulated using a TMM (colormap), compared with the local case (blue line) calculated from Eq. 2. Inverse damping ratio of GEP $\gamma_p^{-1} = \text{Re}(q_{GEP})/\text{Im}(q_{GEP})$, for BBLG (d) and BRTG (e). (f) The electromagnetic field distribution in BBLG, including nonlocal effects. The nonlocal corrections cause less confined modes with increased inverse damping ratio.

in this case, owing to the complexity of the band structure. The dependence of the effective mass on the bias voltage is presented in Fig. 3 (a) and decreases with increasing voltage while $\frac{\hbar^2 q^2}{2m_X}$ increases with increasing voltage, making the nonlocal correction to the conductivity in Eq. 8 more significant.

Substituting the nonlocal conductivity of Eq. 8 into the dispersion relation in Eq. 2 allows us to obtain the more accurate expression to the dispersion relation in the form of the quadratic equation:

$$\frac{\hbar^2 q^2}{2m_X} + \frac{2\sigma_0 f_m}{\varepsilon_0 \varepsilon_{hBN} \varepsilon_{eff} \omega} q - \left(E - E_m + i \frac{\Gamma_m}{2} \right) = 0, \quad (10)$$

with the following physical solution of the nonlocal-corrected dispersion relation:

$$q_{GEP} = -\frac{2\sigma_0 f_m m_X}{\varepsilon_0 \varepsilon_{hBN} \varepsilon_{eff} \hbar^2 \omega} + \sqrt{\left(\frac{2\sigma_0 f_m m_X}{\varepsilon_0 \varepsilon_{hBN} \varepsilon_{eff} \hbar^2 \omega} \right)^2 + \frac{2m_X}{\hbar^2} \left(E - E_m + i \frac{\Gamma_m}{2} \right)}. \quad (11)$$

Fig. 3 (b) and (c) show the comparison between the confinement factors obtained via the local analytic solution (Eq. 2) and nonlocal analytic solution (Eq. 11) for BBLG and BRTG, respectively. It can be seen that the nonlocal dispersion relation yields GEP modes that are less confined by up to an order of magnitude compared to the local model, but that are still larger than the maximal limit of graphene plasmons [32, 61–64]. In addition, the inverse damping ratio, γ_p^{-1} , improves by a factor of four (Fig. 3 (d) and (e)), reaching values that would enable their observation in cryo-SNOM experiments [35]. We note that this behavior of a decreased confinement and increased inverse damping ratio due to nonlocal corrections is consistent with similar observations in other polaritonic systems [10, 57, 61, 68]. The resulting electromagnetic field distribution is presented in Fig. 3 (f), and exhibits the expected decrease in confinement (larger polaritonic wavelength) and increase in the inverse damping ratio (larger propagation length), compared to Fig. 2 (e).

V. EXCITON-HPHP HYBRIDIZATION

The hBN encapsulation plays a major role in obtaining the high-quality electrical and optical response of 2D material systems [21, 35, 37, 60–63, 69]. In addition, it also possesses interesting optical properties by itself since it is a hyperbolic material that supports highly-confined hyperbolic-phonon-polaritons (HPhPs) with low propagation losses [6, 58, 70–75].

The optical response of hBN is commonly described by its frequency-dependent permittivity [6] (appendix

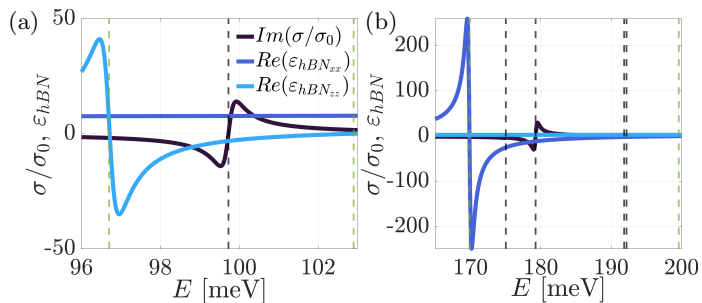


FIG. 4. Conductivity of BBLG for (a) $V = 58$ meV and (b) $V = 115$ meV, with the in-plane and out-of-plane permittivity of hBN. The main and additional exciton energies (dashed black lines) are inside the band limits (dashed green lines).

D). Each permittivity component, separately, is negative in a different spectral region of the optical response, referred to as the Reststrahlen band. Therefore, each Reststrahlen band satisfies the condition $Re(\epsilon_{hBN_{xx}}) \cdot Re(\epsilon_{hBN_{zz}}) < 0$, making the hBN a hyperbolic material in these spectral ranges [76–78]. This condition, leads to a dispersion relation in the form of a hyperboloid isofrequency surface in k space (Eq. F4), enabling the material to support HPhPs, which have the following dispersion relation (for an air/hBN/air structure) [6, 58, 70–75] (appendix G):

$$q_{HPhP}(d) = \frac{i}{d} \sqrt{\frac{\epsilon_{hBN_{zz}}}{\epsilon_{hBN_{xx}}}} \left(2 \arctan \left(\frac{i}{\epsilon_{hBN_{eff}}} \right) + \pi L \right), \quad (12)$$

where d is the hBN thickness and L is an integer signifying the modal order: $L = -1, -2, -3, \dots$ for the lower Reststrahlen band and $L = 0, 1, 2, \dots$ for the upper Reststrahlen band.

The semiconducting state of the BBLG and BRTG has enabled the exploration of their hybridization with a cavity photon by placing them in a microcavity [79, 80]. In our case, however, the BBLG and BRTG exciton's energy can be shifted by changing the value of the bias voltage (appendix B). Thus, by shifting the BBLG or BRTG exciton into the hBN's Reststrahlen bands, multiple hybridizations between the excitons in the BBLG or BRTG and the HPhP in the hBN layers could potentially occur. As an exemplary case, the conductivity of the BBLG and the permittivity of hBN are presented in Fig. 4 (a) and (b) for the lower and upper Reststrahlen bands, respectively, showing positive values of the imaginary part of the conductivity at energies where one of the permittivity components of hBN is negative. The system under investigation is an air/hBN/BBLG/hBN/air structure and using a transmission line model, we can find the dispersion relation of the new structure (appendix H).

A. Symmetric structure

To understand the physical behavior of the system, first we look at a symmetric structure with both hBN layers having a $\frac{d}{2}$ thickness (Fig. 5). Owing to the symmetry around $z = 0$ the solution can be divided into even and odd solutions in terms of the transverse electric field, similarly to HPhP in the air/hBN/air structure introduced in Eq. 12 (appendix G). The dispersion relation of the symmetric structure with $\frac{d}{2} = 50$ nm is presented in Fig. 5 (a) and (b) for the two hBN Reststrahlen bands.

The even solution is given by (appendix I):

$$q_{Hybrid}^{even} = \frac{i}{d + d_\sigma} \sqrt{\frac{\epsilon_{hBN_{zz}}}{\epsilon_{hBN_{xx}}}} \left(2 \arctan \left(\frac{i}{\epsilon_{hBN_{eff}}} \right) + 2\pi L_{even} \right), \quad (13)$$

where $d_\sigma = \frac{i\sigma}{\omega\epsilon_0\epsilon_{hBN_{xx}}}$, which provides the additional polarization current that flows on the BBLG in terms of length (appendix J). It can be seen that the obtained dispersion relation in Eq. 13 is the dispersion relation of even modes of HPhP (Eq. 12), with an effective thickness of $d_{eff} = d + d_\sigma$, i.e.: $q_{Hybrid}^{even} = q_{HPhP}^{even}(d + d_\sigma)$. The analytical solution for the even modes given by Eq. 13 is presented in Fig. 5 (a) and (b) with dashed red lines.

The odd solution is given by (appendix I):

$$q_{Hybrid}^{odd} = \frac{i}{d} \sqrt{\frac{\epsilon_{hBN_{zz}}}{\epsilon_{hBN_{xx}}}} \left(2 \arctan \left(\frac{i}{\epsilon_{hBN_{eff}}} \right) + \pi(2L_{odd} - 1) \right). \quad (14)$$

The odd modes correspond to odd modes of HPhP with thickness of d : $q_{Hybrid}^{odd} = q_{HPhP}^{odd}(d)$. The analytical solution for the odd modes given by Eq. 14 is presented in Fig. 5 (a) and (b) with dashed blue lines. Excellent agreement between the TMM simulation (colormap) and the analytical solution for the even (dashed red line) and odd modes (dashed blue lines), obtained from Eq. 13 and 14, can be seen in Fig. 5.

From Fig. 5 it is clear that the even modes present an anti-crossing between the HPhP (green lines) and the exciton energies (dashed black lines). This anti-crossing, being a signature of hybridization as described in the introduction, is an evidence of the hybridization between the HPhPs and the excitons in the BBLG. Thus, due to the tunability of the excitons in the BBLG, hybridized exciton polaritons appear in both Reststrahlen bands.

The odd modes, however, do not present an anti-crossing behavior as can be seen in Fig. 5, since their transverse electric field is 0 on the BBLG at $z = 0$, yielding no surface current on the BBLG, $J_s = \sigma \mathbb{E}_x(z = 0) = 0$. The transverse magnetic field at $z = 0$ satisfies $\mathbb{H}_y(0^-) - \mathbb{H}_y(0^+) = J_s = 0$, which is the same condition in air/hBN/air structure introduced in Eq. 12. Hence,

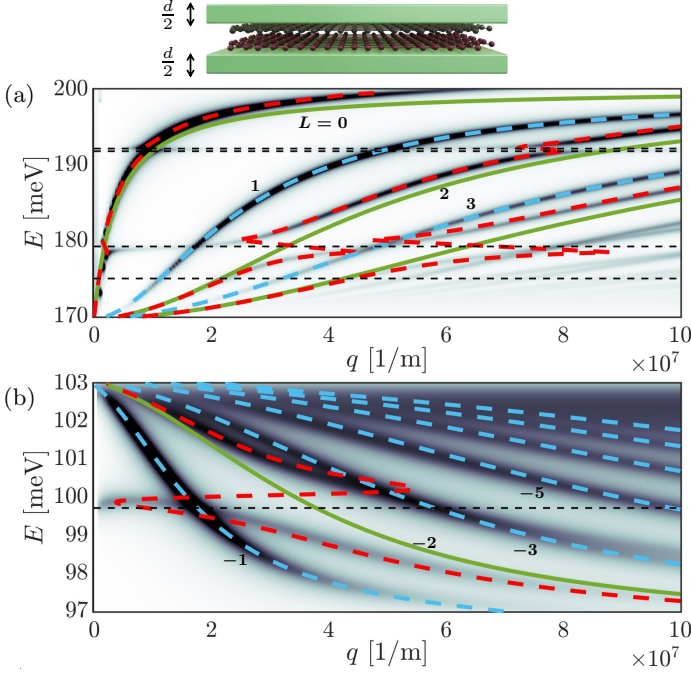


FIG. 5. Hybridization of BBLG excitons and hBN HPhPs for the symmetric structure, with $\frac{d}{2} = 50$ nm. The dispersion relation of the hybridized polariton in the symmetric case for BBLG with $V = 115$ meV (a) and $V = 58$ meV (b), calculated from Eq. 13 (dashed red lines) and Eq. 14 (dashed blue lines), and simulated using TMM (colormap). Even modes of HPhP (green lines), calculated from Eq. 12, and exciton energies of BBLG (dashed black lines) are also plotted. The modal orders L are marked in the figure. The even hybridized modes present an anticrossing behavior between even modes of HPhPs and the excitonic resonances of BBLG while the odd hybridized modes have the dispersion relation of odd HPhPs. The configuration is illustrated above the figure.

the magnetic field is continuous and the odd modes are not affected by the BBLG (Eq. 14).

Note that, unlike the main excitonic resonance, the additional resonances do not present exact anticrossings of the HPhPs dispersion around these resonances, although the general behavior is similar. For instance, in Fig. 5 (a), the even hybridized mode (red curve) that corresponds to the even HPhP (green curve) with $L = 2$ has lower momentum below and above ≈ 192 meV.

The anticrossing between the even HPhPs and the main excitonic resonances can be understood intuitively by examining Eq. 13 (appendix I): the hybridized dispersion relation converges to the dispersion relation of HPhPs far from the excitonic resonances and experiences a decrease or increase momentum compared to HPhPs near the excitonic resonances.

In our case, the lower reststrahlen band only supports one even mode, with modal order $L_{even} = -1$ which correspond to $L = 2L_{even} = -2$ of HPhP (see Fig. 5 (b)), as explained in appendix I.

B. Asymmetric structure

Next, we look at the asymmetric structure with an arbitrary top and bottom hBN thicknesses d_1 and d_2 (Fig. 6). To gain a full understanding of the physical phenomena in the asymmetric structure we choose to analyze a case with an approximate analytical solution, where $d_1, |d_\sigma| \ll d_2$. Using a transmission line model, we can find two sets of solutions for the hybridized modes (appendix K). The dispersion relations of the asymmetric structure in the upper Reststrahlen band are presented in Fig. 6, with $d_1 = 10$ nm and $d_2 = 200$ nm. Fig. 6 (a) shows the existence of two sets of modes, distinguished by their lower and higher momentum.

The first set of modes, is the set of low momentum modes, which satisfy $|k_{hBNz} d_{1,\sigma}| \ll 1$, where k_{hBNz} is the z component of the wavevector in the hBN layers. The dispersion relation of these modes is given by (appendix K):

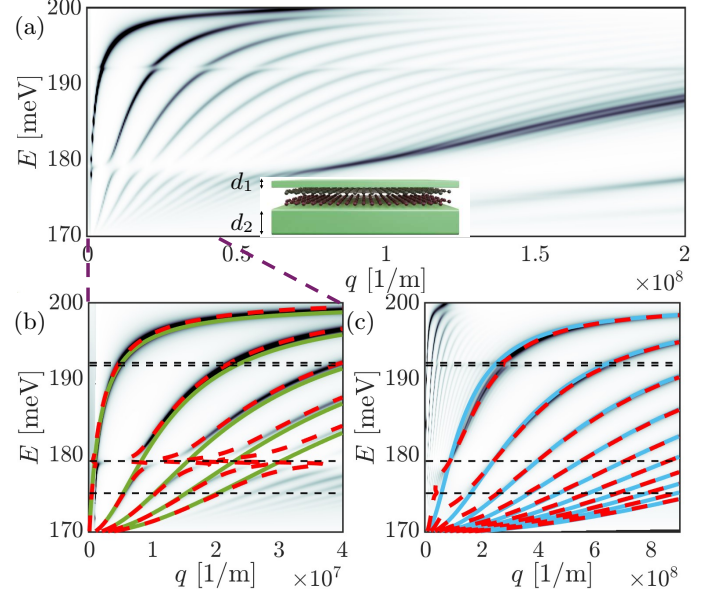


FIG. 6. Hybridization of BBLG excitons and hBN HPhP for the asymmetric structure in the upper Reststrahlen band, with $d_1 = 10$ nm and $d_2 = 200$ nm. (a) The dispersion relation of the hybridized polariton for BBLG with $V = 115$ meV simulated using TMM (colormap) showing two sets of modes. (b) Zoom in on the low momentum modes of panel (a) together with the dispersion relation calculated from Eq. 15 (dashed red lines). Modes of HPhP for hBN with thickness of $d_1 + d_2$ (green lines) and exciton energies of BBLG (dashed black lines) are also plotted. (c) Zoom out to the high momentum modes of panel (a) together with the dispersion relation calculated from Eq. 16 (dashed red lines). Odd modes of HPhP for hBN with thickness of $2d_1$ (blue lines) and exciton energies of BBLG (dashed black lines) are also plotted. The low momentum hybridized modes present an anticrossing behavior while the high momentum hybridized modes cross the main excitonic resonances. The configuration is illustrated as inset.

$$q_{Hybrid}^{low} = \frac{i}{d_1 + d_2 + d_\sigma} \sqrt{\frac{\varepsilon_{hBNzz}}{\varepsilon_{hBNxx}}} \left(2 \arctan \left(\frac{i}{\varepsilon_{hBNeff}} \right) + \pi L_{low} \right). \quad (15)$$

The dispersion relation obtained in Eq. 15 is equivalent to the dispersion relation of HPhP with an effective thickness of $d_{eff} = d_1 + d_2 + d_\sigma$: $q_{Hybrid}^{low} = q_{HPhP}(d_1 + d_2 + d_\sigma)$. The analytical solution for the low momentum modes given by Eq. 15 is presented in Fig. 6 (b) with dashed red lines. The low momentum hybridized modes in the asymmetric structure present the anticrossing that was obtained for the even hybridized modes in the symmetric structure. Here, all the modes experience anticrossing (Fig. 6 (b)), since there is no nullification of the transverse electric field on the BBLG due to symmetry.

The second set of modes is the set of high momentum modes, which satisfies $|k_{hBNz} d_{2,\sigma}| \gg 1$. The dispersion relation of these modes is given by:

$$q_{Hybrid}^{high} = \frac{q_{HPhP}^{odd}(2d_1)}{2} + \sqrt{\left(\frac{q_{HPhP}^{odd}(2d_1)}{2} \right)^2 + \frac{i\omega\varepsilon_0\varepsilon_{hBNzz}}{\sigma d_1}}. \quad (16)$$

The analytical solution for the high momentum modes given by Eq. 16 is presented in Fig. 6 (c) with dashed red lines. Excellent agreement between the TMM simulation (colormap) and the analytical solution (dashed red line), obtained from Eq. 15 and 16, can be seen in Fig. 6.

From Fig. 6 (b), it is clear that the low momentum modes present an anti-crossing between the HPhP (green lines) and the exciton energies (dashed black lines). This anti-crossing is again an evidence of the hybridization. The modes corresponding to q^{high} (Eq. 16), however, cross the main resonances of the BBLG (Fig. 6 (c)), with their momentum being an order of magnitude higher than the q_{low} (Eq. 15) modes.

The dispersion relation in Eq. 16 does not depend on the thickness of the bottom hBN layer, since the conductivity of the BBLG plane is very large relative to the admittance of hBN, and the BBLG serves almost as a short circuit, therefore can be approximately described as a one-sided PEC (appendix K).

The dispersion relations of the asymmetric structure in the lower Reststrahlen band are presented in Fig. 7, with $d_1 = 10$ nm and $d_2 = 200$ nm. Similarly to the upper Reststrahlen band, the lower Reststrahlen band exhibits two sets of modes, distinguished by their lower and higher momentum.

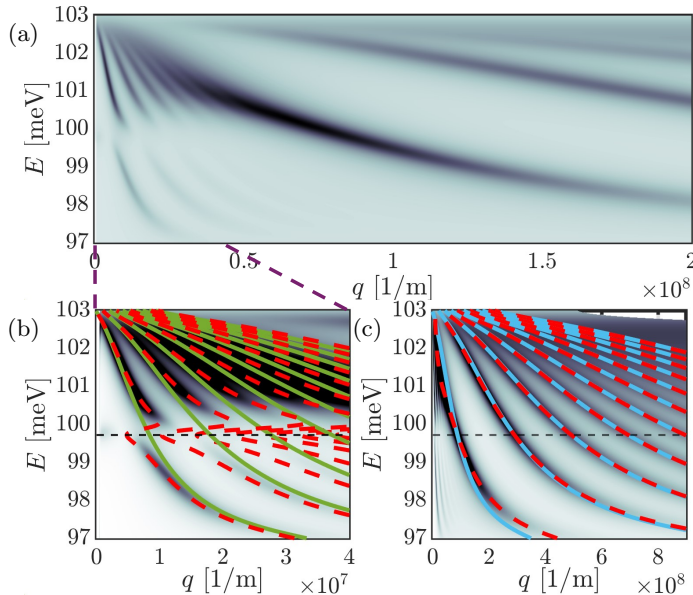


FIG. 7. Hybridization of BBLG excitons and hBN HPhP for the asymmetric structure in the lower Reststrahlen band, with $d_1 = 10$ nm and $d_2 = 200$ nm. (a) The dispersion relation of the hybridized polariton for BBLG with $V = 58$ meV simulated using TMM (colormap) showing two sets of modes. (b) Zoom in on the low momentum modes of panel (a) together with the dispersion relation calculated from Eq. 15 (dashed red lines). Modes of HPhP for hBN with thickness of $d_1 + d_2$ (green lines) and exciton energies of BBLG (dashed black lines) are also plotted. (c) Zoom out to the high momentum modes of panel (a) together with the dispersion relation calculated from Eq. 16 (dashed red lines). Odd modes of HPhP for hBN with thickness of $2d_1$ (blue lines) and exciton energies of BBLG (dashed black lines) are also plotted. The low momentum hybridized modes present an anticrossing behavior while the high momentum hybridized modes cross the main excitonic resonances.

VI. CONCLUSIONS

In conclusion, we have predicted the existence of GEPs collective excitations in BBLG and BRTG at FIR frequencies, which follow a universal dispersion relation law for surface polaritons in 2D excitonic systems. We have studied their electrically tunable polaritonic properties taking into account the appropriate nonlocal corrections, and found that they exhibit promising polariton properties that would enable their observation in cryo-SNOM experiments. Furthermore, we showed that by tuning the excitons spectrally into the Reststrahlen bands of the encapsulating hBN, they can hybridize with HPhPs. Such electrically tunable interband collective excitations in graphene systems may open up new research avenues for polaritonic phenomena that are based on excitonic response.

ACKNOWLEDGMENTS

I.E. acknowledges the support of the European Union (ERC, TOP-BLG, Project No. 101078192). N.M.R.P

acknowledges support from the European Union through project EIC PATHFINDER OPEN project No. 101129661-ADAPTATION, and the Portuguese Foundation for Science and Technology (FCT) in the framework of the Strategic Funding UIDB/04650/2020, COMPETE 2020, PORTUGAL 2020, FEDER, and through project PTDC/FIS-MAC/2045/2021.

Appendix A: Derivation of the optical conductivity

Following from [51], the excitonic optical conductivity is obtained directly from the dynamical equation for the evolution of the off-diagonal (coherences) elements of the density matrix when considering a perturbation by a monochromatic field. This dynamic equation reads

$$i\hbar \frac{d\rho_{cv\mathbf{k}}}{dt} - H_{eh} [\rho_{cv}] = e\mathbf{F} \cdot \mathbf{\Omega}_{cv\mathbf{k}} + ie\mathbf{F} \cdot (\rho_{cv\mathbf{k}})_{;\mathbf{k}}, \quad (\text{A1})$$

where \mathbf{F} is the external optical field, $(\dots)_{;\mathbf{k}}$ denotes the generalized derivative [52], $\mathbf{\Omega}_{cv\mathbf{k}} = \langle v\mathbf{k} | \mathbf{r} | c\mathbf{k} \rangle$ is the \mathbf{k} space interband dipole operator obtained from the Berry connection [51], $\rho_{cv\mathbf{k}}$ represents the off-diagonal elements of the density matrix, also named the coherences, and the electron-hole Hamiltonian H_{eh} has been introduced via its action

$$H_{eh} [\rho_{cv}] = E_{cv\mathbf{k}} \rho_{cv\mathbf{k}} - \sum_{\mathbf{k}'} V_{cv}(\mathbf{k}, \mathbf{k}') \rho_{cv\mathbf{k}'}, \quad (\text{A2})$$

where $V_{cv}(\mathbf{k}, \mathbf{k}')$ represents the \mathbf{k} space electrostatic interaction and the square bracket [...] implies a functional dependence and, therefore, a coupling of all \mathbf{k} points. This equation can be solved iteratively by using the exciton Green's function defined in the time domain via the relation

$$-i\hbar \frac{dG}{dt} + H_{eh} [G] = \delta_{\mathbf{k}, \mathbf{k}'} \delta(t - t'). \quad (\text{A3})$$

Considering the Källén-Lehmann spectral representation [53, 54], this equation has a simple solution in the frequency domain reading

$$G_{\mathbf{k}, \mathbf{k}'}^{\omega} = \sum_n \frac{\psi_{cv\mathbf{k}}^{(n)} \psi_{cv\mathbf{k}'}^{(n)*}}{E_n - \hbar\omega}, \quad (\text{A4})$$

where the eigenstates follow from solving the Bethe-Salpeter equation [41, 42] for the exciton states.

The first-order perturbative correction to the off-diagonal components of the density matrix can then be applied to the calculation of the first-order macroscopic induced current, from which the linear conductivity reads as

$$\boldsymbol{\sigma}^{(1)}(\omega) = \frac{e^2}{8\pi^3 m} \sum_{\mathbf{k}, \mathbf{k}'} \mathbf{p}_{v\mathbf{k}} G_{\mathbf{k}, \mathbf{k}'}^{(\omega)} \mathbf{\Omega}_{cv\mathbf{k}'} + (\omega \rightarrow -\omega)^*, \quad (\text{A5})$$

an excitonic generalization of the free-carrier expressions [52]. Inserting the definition of the Green's function from Eq. A4, and applying the Hamiltonian's commutation relations and some algebraic manipulations, the linear conductivity can be written as

$$\boldsymbol{\sigma}^{(1)}(\omega) = -i \frac{e^2 \hbar}{8\pi^3 m^2} \sum_n \left[E_n \frac{\mathbf{X}_{0n} \mathbf{X}_{n0}}{E_n - \hbar\omega} - (\omega \rightarrow -\omega)^* \right], \quad (\text{A6})$$

where

$$\mathbf{X}_{0n} = i \sum_{\mathbf{k}} \psi_{cv\mathbf{k}}^{(n)} \frac{\mathbf{p}_{cv\mathbf{k}}}{E_{cv\mathbf{k}}}. \quad (\text{A7})$$

The oscillator strength f_n can then be defined as

$$f_n = \frac{\hbar^2}{8\pi^3 m^2} E_n \mathbf{X}_{0n} \mathbf{X}_{n0}, \quad (\text{A8})$$

meaning

$$\sigma^{(1)}(\omega) = 4i\sigma_0 \sum_n \frac{f_n}{E - E_n + i\frac{\Gamma_n}{2}}, \quad (\text{A9})$$

as desired for the resonance part of the conductivity and having included a finite broadening Γ_n .

As the gate voltage will change the bandstructure of both BBLG and BRTG, both the exciton energies and the oscillator strength will be strongly dependent on the gate voltage, as has been previously discussed in the literature [41, 42, 55].

Appendix B: Voltage and Temperature dependence of the conductivity

The conductivity of BBLG and BRTG depends on the value of the bias voltage, as has been previously observed in BBLG and BRTG systems with the electrically tunable bandgap [41, 42]. This property allows us to control the properties of the excitons in the BBLG or BRTG by changing the bias voltage. For instance, the excitons' energies increase with bias voltage [43], allowing shifting the conductivity into a spectral zone of interest, such as the hBN reststrahlen bands (Section V). The oscillator strength and the non-radiative decay rate also increase with the bias voltage, as can be seen in Fig. 1 (c).

Another parameter strongly affecting the excitonic conductivity of the BBLG is the temperature, as has been observed in other 2D semiconductors [56]. We include the effect of temperature on the excitons' linewidth by considering exciton-phonon interactions via the deformation potential mechanism [81–98] (see appendix C), and the resulting temperature-dependent real part of the conductivity are presented in Fig. 1 (d), for ten different temperatures.

It can be seen that the exciton's linewidth, which is proportional to the non-radiative decay rate, is narrowed with decreasing temperature, as has been observed for excitons in 2D semiconductors as well [56]. The linewidth of a resonance determines the optical losses in this spectral range, as discussed in section III.

Appendix C: Temperature effects in the excitons' linewidth

Temperature effects in the excitons' linewidth are included by considering exciton-phonon interactions via

the deformation potential mechanism [81]. Temperature effects are included solely from an intervalley scattering perspective, following from previous works [81], where scattering from acoustic and optical phonons leads to distinct contributions. Following from Fermi's golden rule, the scattering linewidth for acoustic (ac) and optical (op) phonons read

$$\begin{aligned} \gamma_{\text{intra,ac}} &\approx \frac{|\Xi^{(e)} - \Xi^{(h)}|^2}{\rho v_{\text{ac}}^2} \frac{M}{\hbar^2} k_B T \\ \gamma_{\text{intra,op}} &= M \frac{|D^{0,(e)} - D^{0,(h)}|^2}{2\rho \hbar \omega_{\text{op}}} n(\hbar \omega_{\text{op}}), \end{aligned} \quad (\text{C1})$$

respectively. In these expressions, $\Xi^{(e/h)}$ and $D^{0,(e/h)}$ are the first-order acoustic deformation potential and the zero-order optical deformation potential for electron/hole-phonon intravalley scattering, $n(\hbar \omega)$ is the Bose-Einstein distribution, v_{ac} is the speed of sound in the material, $\hbar \omega_{\text{op}}$ is the optical phonon energy, M is the total mass of the electron-hole pair, ρ is the mass density of BBLG, and k_B is the Boltzmann constant. These parameters are frequently computed via DFT studies and can be obtained experimentally, and will strongly depend on the material in question [82–98].

Additionally, we also consider the radiative linewidth of the state n , given by

$$\gamma_{\text{rad}} = \frac{8\pi}{\kappa} \alpha (\hbar v_F)^2 \frac{E'_g + E_n}{E_g^2} |\psi_n(\mathbf{r} = 0)|^2, \quad (\text{C2})$$

where $\alpha \approx 1/137$ is the fine-structure constant, v_F is the Fermi velocity, κ is the dielectric constant of the medium surrounding the layered material, E_g is the non-interacting band gap, E'_g the bandgap with exchange corrections which widen the bandgap, and E_n the binding energy of the excitonic state in question. Finally, the state n is chosen as that which corresponds to the dominant excitonic resonance in the linear conductivity.

Appendix D: Permittivity of hBN

The optical response of hBN is commonly described by its frequency-dependent permittivity [6]:

$$\varepsilon_{hBN_j} = \varepsilon_{hBN_j^\infty} \left(1 + \frac{\omega_{LO,j}^2 - \omega_{TO,j}^2}{\omega_{TO,j}^2 - \omega^2 - i\omega\Gamma_j} \right), \quad (\text{D1})$$

where $j = xx, zz$ is the in-plane or out-of-plane direction, $\varepsilon_{hBN_j^\infty}$ is the background permittivity, $\omega_{LO,j}$ and $\omega_{TO,j}$ are the longitudinal and transverse optical phonon frequencies, respectively, and Γ_j is the decay rate.

Appendix E: Transmission Line Model

The transmission line model is a useful method for solving 3D wave problems with vector fields using a sim-

ple 1D problem with scalars. We assume a time dependence of $e^{-i\omega t}$, and due to symmetry in the $x - y$ plane in the structures investigated in our work, we can take the propagation direction to be \hat{x} and assume uniformity of the fields in the \hat{y} direction without loss of generality. Due to the continuity of the transverse electric field on the discontinuities planes of constant z in the transmission between different materials, we can assume a transverse dependence of e^{iqx} , yielding the TM fields: $\mathbb{E} = (\hat{x}\mathbb{E}_x(z) + \hat{z}\mathbb{E}_z(z))e^{iqx}$ and $\mathbb{H} = \hat{y}\mathbb{H}_y(z)e^{iqx}$. Using Maxwell's equations, it can be shown that the above transverse electric and magnetic fields, $\mathbb{E}_x(z)$ and $\mathbb{H}_y(z)$, satisfy the telegraph equations describing voltage and current in a transmission line [99], and will be referred to as voltage and current in the further discussion. The transmission line supports forward and backward propagating waves, with a longitudinal dependence of $e^{\pm ik_{i_z}z}$, where k_{i_z} is the z component of the wavevector in the i th layer. The characteristic admittance of a transmission line describes the ratio between the current and the voltage of a forward propagating wave and equals to minus this ratio for a backward propagating wave. Using Maxwell's equations, the characteristic admittance of the i th layer is given by:

$$Y_i = \frac{\mathbb{H}_y^+(z)}{\mathbb{E}_x^+(z)} = -\frac{\mathbb{H}_y^-(z)}{\mathbb{E}_x^-(z)} = \frac{\omega\varepsilon_0\varepsilon_{i_{xx}}}{k_{i_z}}, \quad (\text{E1})$$

where $\varepsilon_{i_{xx}}$ is the in-plane permittivity of the i th layer. The z dependent admittance is defined as the ratio between the current and the voltage: $Y(z) = \frac{\mathbb{H}_y(z)}{\mathbb{E}_x(z)}$. If the i th layer is half infinite for $z \rightarrow \pm\infty$, then there is only a backward (or forward) propagating wave, and in this layer: $Y(z) = \pm Y_i$. The dispersion relation of polaritons, describing eigen modes of electromagnetic waves in the structure, can be found by solving the transverse resonance equation, obtained by equalizing the solutions of the z dependent admittance at a point z_0 that satisfy the boundary conditions for $z > z_0$ and $z < z_0$. Assuming the graphene system in our structures is located at $z = 0$, the boundary condition at $z = 0$ is given by: $\mathbb{H}_y(0^-) - \mathbb{H}_y(0^+) = \sigma\mathbb{E}_x(0)$, which in terms of admittances is given by: $Y(0^-) - Y(0^+) = \sigma$.

Appendix F: Derivation of the dispersion relation of GEP

Here we analyze the polaritonic properties of the GEPs in the two systems under study by analytically deriving the dispersion relation of the polaritons using a transmission line model (appendix E), for a structure of hBN/graphene system/hBN (where the graphene system is either BBLG or BRTG). In evaluating the dispersion relation of the two systems, the BBLG and the BRTG layers are modeled as infinitesimal layers with surface conductivity σ . The conductivity, under the assumption of a thin layer, is related to the permittivity ε through

$\sigma = -i\omega\varepsilon_0(\varepsilon - 1)d$, where $\omega = \frac{E}{\hbar}$ is the frequency and d is the thickness of the material. The condition of the negative real part of their permittivity is therefore equivalent to the positive imaginary part of their conductivity, under the assumption $\varepsilon \gg 1$. For simplicity, we assume that the hBN layers are semi-infinite in the $\pm z$ directions and that the systems are infinite in the $x - y$ plane.

The z dependent admittance at $z \neq 0$ is given by $Y(z) = \text{sign}(z)Y_{hBN}$, since the hBN layers are half infinite for $z \rightarrow \pm\infty$ (appendix E). By inserting this relation into the boundary condition at $z = 0$, we obtain the transverse resonance equation:

$$2Y_{hBN} + \sigma = 0, \quad (\text{F1})$$

with

$$Y_{hBN} = \frac{\omega\varepsilon_0\varepsilon_{hBN_{xx}}}{k_{hBN_z}}, \quad (\text{F2})$$

where Y_{hBN} is the characteristic admittance of hBN, $\varepsilon_{hBN_{xx}}$ is the in-plane x permittivity component of hBN, and k_{hBN_z} is the z component of the wavevector in the hBN layers. Combining Eq. F1 and F2 gives the known equation for a TM polariton in a 2D infinitesimal layer (Eq. 2), as have been obtained for graphene plasmons in monolayer graphene [100] and for exciton polaritons in monolayer TMD [56], for example.

The Transverse electric field distribution of GEP is given by:

$$\mathbb{E}_x(x, z) = \mathbb{E}_x(0, 0)e^{iq_{GEP}x + ik_{hBN_z}|z|}, \quad (\text{F3})$$

where q_{GEP} is the component of the wavevector in the x direction (the momentum). The coordinate system is defined as illustrated above Fig. 1, and the graphene systems are at $z = 0$. The electric field distribution in Eq. F3 is presented in Fig. 2 (e). The momentum is related to k_{hBN_z} by [76–78]:

$$\frac{q_{GEP}^2}{\varepsilon_{hBN_{zz}}} + \frac{k_{hBN_z}^2}{\varepsilon_{hBN_{xx}}} = k_0^2, \quad (\text{F4})$$

where $\varepsilon_{hBN_{zz}}$ is the out-of-plane z permittivity component of hBN, $k_0 = \frac{\omega}{c}$ is the free-space wavenumber and c is the speed of light in vacuum. Since polaritons are characterized by high momentum, we can approximate $q_{GEP} \gg \sqrt{\varepsilon_{hBN_{zz}}}k_0$, which leads to $k_{hBN_z} \approx iq_{GEP}\sqrt{\frac{\varepsilon_{hBN_{xx}}}{\varepsilon_{hBN_{zz}}}}$.

From the dispersion relation obtained using the calculation in this appendix, approximated expressions for the confinement factor (Eq. 5) and inverse damping ratio (Eq. 6) were derived in section III. We note that these are only valid where the polariton exists. At energies lower than the main resonance, it seems that the confinement is negative, and the systems have gains instead of losses. Nevertheless, the imaginary part of the conductivity is

negative at $E < E_m$ (Fig. 1 (a) and (b)), and there are no GEPs. These equations also are only valid within the peak of the main resonance and describe the linear part (at low energies) of the confinement factor and the inverse damping ratio in Fig. 2.

Eq. 6 comes out independent on the properties of hBN. This is a result of the assumption that $q_{GEP} \gg \sqrt{\varepsilon_{hBN_{zz}}}k_0$. The polaritons are so confined to the graphene systems, that the surrounding medium barely affects their losses, in terms of inverse damping ratio.

Appendix G: Transverse resonance equation of HPhP

We now investigate the structure of air/hBN/air, where the thickness of the hBN is d . The z dependent admittance at the air layers are given by $Y(z \geq \frac{d}{2}) = Y_{air}$ and $Y(z \leq -\frac{d}{2}) = -Y_{air}$, since the air layers are half infinite for $z \rightarrow \pm\infty$. The z dependent admittance at the hBN layer is given by:

$$Y(z) = \frac{\mathbb{H}_y^+(z) + \mathbb{H}_y^-(z)}{\mathbb{E}_x^+(z) + \mathbb{E}_x^-(z)} = Y_{hBN} \frac{\mathbb{H}_y^+(z) + \mathbb{H}_y^-(z)}{\mathbb{H}_y^+(z) - \mathbb{H}_y^-(z)}. \quad (\text{G1})$$

Since the transverse field are continuous between layers, so is the z dependent admittance. Therefore, the boundary condition at $z = \frac{d}{2}$ gives:

$$Y\left(\frac{d}{2}\right) = Y_{hBN} \frac{\mathbb{H}_y^+(\frac{d}{2}) + \mathbb{H}_y^-(\frac{d}{2})}{\mathbb{H}_y^+(\frac{d}{2}) - \mathbb{H}_y^-(\frac{d}{2})} = Y_{air}. \quad (\text{G2})$$

Eq. G2 gives the reflection coefficient for the current:

$$r\left(\frac{d}{2}\right) = \frac{\mathbb{H}_y^-(\frac{d}{2})}{\mathbb{H}_y^+(\frac{d}{2})} = \frac{Y_{air} - Y_{hBN}}{Y_{air} + Y_{hBN}}. \quad (\text{G3})$$

Inserting the reflection coefficient and the z dependence of the waves into G1 at $z = 0$ gives the tangent equation:

$$\begin{aligned} Y(0) &= Y_{hBN} \frac{\mathbb{H}_y^+(\frac{d}{2})e^{-ik_{hBNz}\frac{d}{2}} + \mathbb{H}_y^-(\frac{d}{2})e^{ik_{hBNz}\frac{d}{2}}}{\mathbb{H}_y^+(\frac{d}{2})e^{-ik_{hBNz}\frac{d}{2}} - \mathbb{H}_y^-(\frac{d}{2})e^{ik_{hBNz}\frac{d}{2}}} = \\ &= Y_{hBN} \frac{Y_{air} - iY_{hBN}\tan(k_{hBNz}\frac{d}{2})}{Y_{hBN} - iY_{air}\tan(k_{hBNz}\frac{d}{2})}. \end{aligned} \quad (\text{G4})$$

Due to the symmetry of the structure around the z axis, it supports even modes (even voltage around the z axis) and odd modes (odd voltage around the z axis). We note that the parity of the current is opposite to the parity of the voltage in TM polarization. Since the transverse fields are continuous at $z = 0$, the even modes satisfy a nullification of the current at $z = 0$ and $Y(z =$

$0) = 0$ and the odd modes satisfy a nullification of the voltage at $z = 0$ and $Y^{-1}(z = 0) = 0$.

The transverse resonance equation for the even modes is given by $Y_{air} - iY_{hBN}\tan(k_{hBNz}\frac{d}{2}) = 0$ and for the odd modes is given by $Y_{hBN} - iY_{air}\tan(k_{hBNz}\frac{d}{2}) = 0$. From the transverse resonance equations, the dispersion relation in Eq. 12 can be obtained, with even modal orders for the even modes and odd modal orders for the odd modes.

Appendix H: Transverse resonance equation of the Hybridized Modes

We now investigate a structure of air/hBN/BBLG/hBN/air. The z dependent admittances at the air layers are given by $Y(z \geq d_2) = Y_{air}$ and $Y(z \leq -d_1) = -Y_{air}$, since the air layers are half infinite for $z \rightarrow \pm\infty$. Similarly to the derivation of Eq. G4, the z dependent admittance at $z = 0^+$ in the bottom hBN layer is given by:

$$Y(0^+) = Y_{hBN} \frac{Y_{air} - iY_{hBN}\tan(k_{hBNz}d_2)}{Y_{hBN} - iY_{air}\tan(k_{hBNz}d_2)}, \quad (\text{H1})$$

where $Y_{air} = \frac{\omega\varepsilon_0}{k_{airz}}$ is the characteristic admittance of air, k_{airz} is the z component of the wavevector in the air layers and d_1 and d_2 are the thicknesses of the top and bottom hBN layers. The values of d_1 and d_2 do not have strict limitations generally, although we will derive analytical expression for two different cases, which limit the value of thicknesses for our discussion.

Similarly, the z dependent admittance at $z = 0^-$ is given by:

$$Y(0^-) = Y_{hBN} \frac{Y_{air} - iY_{hBN}\tan(k_{hBNz}d_1)}{Y_{hBN} - iY_{air}\tan(k_{hBNz}d_1)}. \quad (\text{H2})$$

By inserting the relations in Eq. H1 and H2 into the boundary condition at $z = 0$, we obtain the transverse resonance equation:

$$\begin{aligned} &Y_{hBN} \frac{Y_{air} - iY_{hBN}\tan(k_{hBNz}d_1)}{Y_{hBN} - iY_{air}\tan(k_{hBNz}d_1)} + \\ &+ Y_{hBN} \frac{Y_{air} - iY_{hBN}\tan(k_{hBNz}d_2)}{Y_{hBN} - iY_{air}\tan(k_{hBNz}d_2)} + \sigma = 0. \end{aligned} \quad (\text{H3})$$

Appendix I: Dispersion Relation of the Symmetric Hybridized Modes

The odd modes of the hybridized polaritons in the symmetric case satisfy a nullification of the voltage at $z = 0$ and $Y^{-1}(z = 0) = 0$. Therefore, they are obtained by equalizing the denominator Eq. H1 or H2 to 0, which

gives the transverse resonance equation of odd modes of HPhPs.

The even modes of the hybridized polaritons in the symmetric case do not satisfy a nullification of the current at $z = 0$ due to the presence of the graphene system. Therefore, we cannot use the simplification of the symmetric structures here. The transverse resonance equation of even modes is obtained by setting $d_1 = d_2 = \frac{d}{2}$ in Eq. H3. To derive the dispersion relation we use the trigonometric identity $\tan(\theta_1 + \theta_2) = \frac{\tan(\theta_1) + \tan(\theta_2)}{1 - \tan(\theta_1)\tan(\theta_2)}$ with $\theta_1 = k_{hBN_z} \frac{d}{2}$ and $\theta_2 = \arctan\left(i \frac{Y_{air}}{Y_{hBN}}\right)$ on the transverse resonance equation and obtain:

$$\tan\left(k_{hBN_z} \frac{d}{2} + \arctan\left(i \frac{Y_{air}}{Y_{hBN}}\right)\right) = \frac{\sigma}{2iY_{hBN}}. \quad (\text{I1})$$

We now use the arctan operator on both sides of Eq. I1 and use the approximation $\arctan\left(\frac{\sigma}{2iY_{hBN}}\right) \approx \frac{\sigma}{2iY_{hBN}}$ due to assumption of $|\frac{\sigma}{Y_{hBN}}| \ll 1$:

$$k_{hBN_z} \frac{d}{2} + \arctan\left(i \frac{Y_{air}}{Y_{hBN}}\right) + \pi L_{even} = \frac{\sigma}{2iY_{hBN}}, \quad (\text{I2})$$

where L_{even} is an integer that satisfies $|\frac{\sigma}{Y_{hBN}}| \ll 1$. We now define $d_\sigma = \frac{i\sigma}{\omega\varepsilon_0\varepsilon_{hBN_{xx}}}$ and write $\frac{\sigma}{Y_{hBN}} = -ik_{hBN_z} d_\sigma$. Using the approximation $q \gg \sqrt{\varepsilon_{hBN_{zz}}} k_0$, we can write $k_{hBN_z} \approx iq\sqrt{\frac{\varepsilon_{hBN_{xx}}}{\varepsilon_{hBN_{zz}}}}$ and $k_{air_z} \approx iq$, and therefore $\frac{Y_{air}}{Y_{hBN}} = \varepsilon_{hBN_{eff}}^{-1}$. Setting these relations in Eq. I2 gives the dispersion relation of the even hybridized modes in Eq. 13. For the parameters of Fig. 5 (a), the lower Reststrahlen band only supports one even mode, with modal order $L_{even} = -1$ which corresponds to $L = 2L_{even} = -2$ of HPhP. This is the only even mode that solves Eq. H3 with the parameters of this case since the assumption of $|\frac{\sigma}{Y_{hBN}}| \ll 1$ does not hold for the other modes.

The analytical dispersion relation in Eq. 13 was derived under the approximation of $|k_{hBN_z} d_\sigma| \ll 1$, which can be written as $|\frac{\sigma}{Y_{hBN}}| \ll 1$: the BBLG plane has a very low admittance relative to the hBN, and therefore the influence of the BBLG can be considered as a small correction to the dispersion relation of the HPhPs.

Far from the excitonic resonances of the BBLG, d_σ is negligible, and the even hybridized modes converge to even modes of HPhPs. Near the excitonic resonances, the contribution of the conductivity is significant, and d_σ effectively increases or decreases the thickness of the hBN layers, according to the signs of the conductivity of BBLG and of the in-plane permittivity of hBN. In the lower Reststrahlen band $Re(\varepsilon_{hBN_{xx}}) > 0$ (Fig. 4 (a)), therefore below the main excitonic resonance of BBLG where $Im(\sigma) < 0$: $d_\sigma > 0$ (Fig. 8 (a)) and $d_{eff} > d$ and above the main excitonic resonance of BBLG where $Im(\sigma) > 0$: $d_\sigma < 0$ and $d_{eff} < d$. In the upper Reststrahlen band $Re(\varepsilon_{hBN_{xx}}) < 0$ (Fig. 4 (a)), therefore below the main excitonic resonance of BBLG $d_{eff} < d$ and

above it $d_{eff} > d$. From Eq. 12 it is clear that the momentum of HPhP is inverse to the thickness of the hBN layer. Hence, when $d_{eff} < d$, the even hybridized modes have an increased momentum compared to the HPhPs, and when $d_{eff} > d$, the even hybridized modes have a decreased momentum compared to the HPhPs (Fig. 5). The discussion above is summarized in table I.

		$Re(\varepsilon_{hBN_{xx}})$	$Im(\sigma)$	$Re(d_\sigma) = Re(d_{eff}) - d$	$Re(q_{Hybrid}^{even} - q_{HPhP}^{even})$
Lower Reststrahlen band	Below main res.	+	-	+	-
	Above main res.	+	+	-	+
Upper Reststrahlen band	Below main res.	-	-	-	+
	Above main res.	-	+	+	-

TABLE I. Explanation of the anticrossing behavior of the even modes of the hybridized polariton in the symmetric structure. The + and - signs describe the signs of the quantities in the different spectral regions.

In the upper reststrahlen band, the even hybridized modes do not converge with the even HPhPs at high energies, as can be seen for the $L = 0$ mode in Fig. 5 (a). Although these energies are far from the excitonic resonances, they are near the in-plane longitudinal optical phonon frequency of the hBN, where the in-plane permittivity of hBN is very small and therefore d_σ is not negligible.

Appendix J: The additional polarization current

In order to understand the meaning of d_σ , we use Ampere's law in the x direction around $z = 0$:

$$-\partial_z \mathbb{H}_y = -i\omega\varepsilon_0\varepsilon_{hBN_{xx}} \mathbb{E}_x + J, \quad (\text{J1})$$

where J is the current density due to the presence of the BBLG. The surface current density on the BBLG $J_s = J \cdot d_{BBLG}$ is given by Ohm's law $J_s = \sigma \mathbb{E}_x$, where d_{BBLG} is the thickness of the BBLG. Therefore, Eq. J1 can be written as:

$$-\partial_z \mathbb{H}_y = -i\omega\varepsilon_0\varepsilon_{hBN_{xx}} \left(1 + \frac{d_\sigma}{d_{BBLG}}\right) \mathbb{E}_x. \quad (\text{J2})$$

The parameter d_σ therefore provides the additional polarization current that flows on the BBLG in terms of length.

The frequency dependence of d_σ is presented in Fig 8 (a) and (b), for the lower Reststrahlen band with $V =$

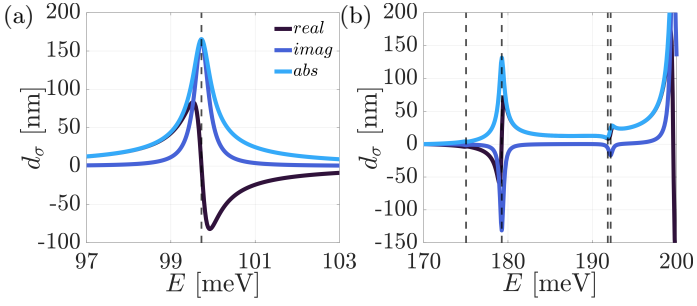


FIG. 8. d_σ for (a) $V = 58$ meV and (b) $V = 115$ meV.

58 meV and for the upper Reststrahlen band with $V = 115$ meV, respectively.

Appendix K: Dispersion Relation of the Asymmetric Hybridized Modes

Under the chosen conditions of $d_1, |d_\sigma| \ll d_2$, the transverse resonance equation has two sets of solutions. The derivation of the set of low momentum modes is similar to the derivation of the even modes in the symmetric case. Similarly to Eq. I1 we can write:

$$\begin{aligned} & \tan\left(k_{hBN_z} d_2 + \arctan\left(i \frac{Y_{air}}{Y_{hBN}}\right)\right) \\ &= -\tan\left(k_{hBN_z} d_1 + \arctan\left(i \frac{Y_{air}}{Y_{hBN}}\right)\right) + \frac{\sigma}{iY_{hBN}}. \end{aligned} \quad (\text{K1})$$

We now use the arctan operator on both sides of Eq. K1 and use the approximation $\arctan(x) \approx x$ with x being the right-hand-side of Eq. K1, due to assumptions of $|\frac{\sigma}{Y_{hBN}}| \ll 1$ and $|k_{hBN_z} d_1| \ll 1$. We then use the same approximation with $x = k_{hBN_z} d_1 + \arctan(i \frac{Y_{air}}{Y_{hBN}})$, and obtain:

$$k_{hBN_z} (d_1 + d_2) + 2 \arctan\left(i \frac{Y_{air}}{Y_{hBN}}\right) + \pi L_{low} = \frac{\sigma}{iY_{hBN}}. \quad (\text{K2})$$

Using $\frac{\sigma}{Y_{hBN}} = -ik_{hBN_z} d_\sigma$, $\frac{Y_{air}}{Y_{hBN}} = \varepsilon_{hBN_{eff}}^{-1}$ and $k_{hBN_z} \approx iq \sqrt{\frac{\varepsilon_{hBN_{xx}}}{\varepsilon_{hBN_{zz}}}}$ we obtain the dispersion relation of the low modes in Eq. 15.

To derive the dispersion relation of the set of high momentum modes we start by using the assumption that d_2 is larger than all quantities with length dimensions, therefore the bottom layer can be approximated as half infinite and $Y(0^+) = Y_{hBN}$. Using the assumption of $|\frac{\sigma}{Y_{hBN}}| \gg 1$, we can neglect $Y(0^+)$, and the transverse resonance equation is therefore $Y(0^-) + \sigma = 0$, where $Y(0^-)$ is given by Eq. H2. Now, similarly to Eq. I1 we can write:

$$\tan\left(k_{hBN_z} d_1 + \arctan\left(i \frac{Y_{air}}{Y_{hBN}}\right)\right) = \frac{\sigma}{iY_{hBN}}. \quad (\text{K3})$$

We now use the arctan operator on both sides of Eq. K3 and use the approximation $\arctan(\frac{\sigma}{iY_{hBN}}) \approx \frac{\pi}{2} - \frac{iY_{hBN}}{\sigma}$ due to assumption of $|\frac{\sigma}{Y_{hBN}}| \gg 1$:

$$k_{hBN_z} d_1 + \arctan\left(i \frac{Y_{air}}{Y_{hBN}}\right) + \pi L_{high} = \frac{\pi}{2} - \frac{iY_{hBN}}{\sigma}. \quad (\text{K4})$$

Using $\frac{\sigma}{Y_{hBN}} = -ik_{hBN_z} d_\sigma$ and $\frac{Y_{air}}{Y_{hBN}} = \varepsilon_{hBN_{eff}}^{-1}$, and multiplying Eq. K4 by k_{hBN_z} , we obtain a quadratic equation in terms of k_{hBN_z} :

$$k_{hBN_z}^2 d_1 - k_{hBN_z} \cdot k_{hBN_z}^{HP, odd}(2d_1) \cdot d_1 + (d_\sigma)^{-1} = 0, \quad (\text{K5})$$

with

$$\begin{aligned} & k_{hBN_z}^{HP, odd}(2d_1) = \\ &= -\frac{1}{2d_1} \left(2 \arctan\left(\frac{i}{\varepsilon_{hBN_{eff}}}\right) + \pi(2L_{high} - 1) \right), \end{aligned} \quad (\text{K6})$$

where $k_{hBN_z}^{HP, odd}(2d_1)$ is the z component of the wavevector in hBN for odd modes of HPhP with hBN with thickness $2d_1$. Solving the above equation and setting $k_{hBN_z} \approx iq \sqrt{\frac{\varepsilon_{hBN_{xx}}}{\varepsilon_{hBN_{zz}}}}$ gives the dispersion relation of the high modes in Eq. 16.

The dispersion relation in Eq. 16 does not depend on the thickness of the bottom hBN layer. Since d_2 is much larger than all quantities with length dimensions, we can assume that the thicker hBN slab is half infinite, making its contribution negligible. Another explanation is that the conductivity of the BBLG plane is very large relative to the admittance of hBN since the condition $|k_{hBN_z} d_\sigma| \gg 1$ can be written as $|\frac{\sigma}{Y_{hBN}}| \gg 1$, and the BBLG serves almost as a short circuit, therefore can be approximately described as a one-sided PEC. For high values of the conductivity and for high modal orders, the assumption $|k_{hBN_z} d_\sigma| \gg 1$ is more accurate, and the hybridized modes converge to odd modes of HPhP with thickness $2d_1$: $q_{Hybrid}^{high} = q_{HPhP}^{odd}(2d_1)$, and are not affected by the BBLG (Fig. 7 (c) and Fig. 6 (c)). This can be understood through the validity of the approximation of the BBLG as a PEC, which divides the structure into two areas. For $z > 0$ there is half infinite hBN which cannot support guided modes. For $z < 0$ there is a hBN slab with thickness d_1 with air on one side and a high conductivity on the other. In this area, the solution is equivalent to a finite slab with $2d_1$ where the transverse electric field is zero at $z = 0$ - odd modes. The high momentum modes present around the main resonance an

opposite behavior compared to the anticrossing observed for the low momentum modes. These modes exist in the crossing between the HPhP and the main excitonic resonances, where the conductivity is high and the hybridized modes converge to HPhPs. At energies far from the main resonance, where the conductivity is lower, the influence of the BBLG is more significant.

Nevertheless, it can be seen in Fig. 6 (c) that around the additional resonance at ≈ 192 meV an "anticrossing" behavior occurs (similar to 5 (a) for $L = 2$ at the same energy), compared to the crossing of the main resonances. Again, this is not an exact anticrossing behavior since the hybridized modes remain on the same side of the HPhP dispersion curves. To understand this phenomenon, we should examine Eq. 16 around the resonances. Near the main resonance, the imaginary part of the BBLG conductivity changes signs (Fig. 4 (b)), so the hybridized modes added momentum, with respect to the HPhP, also changes its sign when the energy is below or above the main resonance, resulting in a crossing of the HPhP dispersion. Near the higher-order resonances, the imaginary part of the conductivity remains positive, yielding a larger momentum for the hybridized mode compared with HPhP both above and below the resonance. Around this resonance there is, however, a sharp transition in the value of σ , resulting in the "anticrossing" behavior.

Appendix L: Excitonic effective mass in BBLG

We will now showcase the derivation of the excitonic effective mass for a BBLG system. This derivation is

focused on the two bands closest to the bandgap of the system as this band pair dominates the excitonic states for low gate voltages and, more importantly, for photon energies below the value of the second bandgap [55].

From the two discussed bands, with dispersion relations

$$E_{\pm}(k) = \frac{\pm \sqrt{2k^2 \hbar^2 v_F^2 + 2V^2 + \gamma_1^2} - \sqrt{\gamma_1^4 + 4k^2 \hbar^2 v_F^2 (4V^2 + \gamma_1^2)}}{\sqrt{2}}, \quad (\text{L1})$$

the effective mass will be given by

$$\frac{1}{m_X} = \frac{1}{\hbar^2} \left[\left. \frac{\partial^2 E_+(k)}{\partial k^2} \right|_{k=k_{\min}} - \left. \frac{\partial^2 E_-(k)}{\partial k^2} \right|_{k=k_{\max}} \right], \quad (\text{L2})$$

where k_{\max} and k_{\min} are the locations of the maximum and minimum of the valence and conduction bands, respectively. As the band extremes are located at

$$k_{\max} = k_{\min} = \frac{V \sqrt{1 + \frac{\gamma_1^2}{4V^2 + \gamma_1^2}}}{\hbar v_F}, \quad (\text{L3})$$

the exciton effective mass will therefore be

$$m_X = \frac{\gamma_1 (4V^2 + \gamma_1^2)^{3/2}}{16V v_F^2 (2V^2 + \gamma_1^2)}. \quad (\text{L4})$$

-
- [1] D. N. Basov, A. Asenjo-Garcia, P. J. Schuck, X. Zhu, and A. Rubio, Polariton panorama, *Nanophotonics* **10**, 549 (2020).
- [2] D. N. Basov, M. M. Fogler, and F. J. García De Abajo, Polaritons in van der Waals materials, *Science* **354**, 10.1126/SCIENCE.AAG1992 (2016).
- [3] T. Low, A. Chaves, J. D. Caldwell, A. Kumar, N. X. Fang, P. Avouris, T. F. Heinz, F. Guinea, L. Martin-Moreno, and F. Koppens, Polaritons in layered two-dimensional materials, *Nature Materials* 2016 16:2 **16**, 182 (2016).
- [4] M. Jablan, H. Buljan, and M. Soljačić, Plasmonics in graphene at infrared frequencies, *Physical Review B - Condensed Matter and Materials Physics* **80**, 245435 (2009).
- [5] F. H. Koppens, D. E. Chang, and F. J. García De Abajo, Graphene plasmonics: A platform for strong light-matter interactions, *Nano Letters* **11**, 3370 (2011).
- [6] S. Dai, Z. Fei, Q. Ma, A. S. Rodin, M. Wagner, A. S. McLeod, M. K. Liu, W. Gannett, W. Regan, K. Watanabe, T. Taniguchi, M. Thiemens, G. Dominguez, A. H. Castro Neto, A. Zettl, F. Keilmann, P. Jarillo-Herrero, M. M. Fogler, and D. N. Basov, Tunable phonon polaritons in atomically thin van der Waals crystals of boron nitride, *Science* **343**, 1125 (2014).
- [7] J. D. Caldwell, L. Lindsay, V. Giannini, I. Vurgaftman, T. L. Reinecke, S. A. Maier, and O. J. Glembocki, Low-loss, infrared and terahertz nanophotonics using surface phonon polaritons, *Nanophotonics* **4**, 44 (2015).
- [8] J. D. Caldwell, A. V. Kretinin, Y. Chen, V. Giannini, M. M. Fogler, Y. Francescato, C. T. Ellis, J. G. Tischler, C. R. Woods, A. J. Giles, M. Hong, K. Watanabe, T. Taniguchi, S. A. Maier, and K. S. Novoselov, Sub-diffractive volume-confined polaritons in the natural hyperbolic material hexagonal boron nitride, *Nature Communications* 2014 5:1 **5**, 1 (2014).
- [9] C. Schneider, M. M. Glazov, T. Korn, S. Höfling, and B. Urbaszek, Two-dimensional semiconductors in the regime of strong light-matter coupling, *Nature Communications* 2018 9:1 **9**, 1 (2018).
- [10] S. A. Maier, Plasmonics: Fundamentals and applications, *Plasmonics: Fundamentals and Applications*, 1 (2007).
- [11] W. L. Barnes, A. Dereux, and T. W. Ebbesen, Surface plasmon subwavelength optics, *Nature* 2003 424:6950 **424**, 824 (2003).
- [12] T. W. Ebbesen, H. J. Lezec, H. F. Ghaemi, T. Thio, and P. A. Wolff, Extraordinary optical transmission through sub-wavelength hole arrays, *Nature* 1998 391:6668 **391**, 667 (1998).
- [13] I. Epstein, Y. Tsur, and A. Arie, Surface-plasmon wave-

- front and spectral shaping by near-field holography, *Laser & Photonics Reviews* **10**, 360 (2016).
- [14] V. M. Agranovich, *Surface Polaritons* (Elsevier Science, 2014) p. 734.
- [15] J. Lagois and B. Fischer, Experimental Observation of Surface Exciton Polaritons, *Physical Review Letters* **36**, 680 (1976).
- [16] J. Lagois and B. Fischer, Dispersion theory of surface-exciton polaritons, *Physical Review B* **17**, 3814 (1978).
- [17] S. A. Elrafei, T. V. Raziman, S. De Vega, F. J. García De Abajo, and A. G. Curto, Guiding light with surface exciton-polaritons in atomically thin superlattices, *Nanophotonics* **13**, 3101 (2024).
- [18] Y. Tokura and T. Koda, Surface Exciton Polariton in ZnO, <https://doi.org/10.1143/JPSJ.51.2934> **51**, 2934 (1982).
- [19] J. Chen, M. Badioli, P. Alonso-González, S. Thongrattanasiri, F. Huth, J. Osmond, M. Spasenović, A. Centeno, A. Pesquera, P. Godignon, A. Zurutuza Elorza, N. Camara, F. J. García, R. Hillenbrand, and F. H. Koppens, Optical nano-imaging of gate-tunable graphene plasmons, *Nature* 2012 487:7405 **487**, 77 (2012).
- [20] Z. Fei, A. S. Rodin, G. O. Andreev, W. Bao, A. S. McLeod, M. Wagner, L. M. Zhang, Z. Zhao, M. Thiems, G. Dominguez, M. M. Fogler, A. H. Castro Neto, C. N. Lau, F. Keilmann, and D. N. Basov, Gate-tuning of graphene plasmons revealed by infrared nano-imaging, *Nature* 2012 487:7405 **487**, 82 (2012).
- [21] N. C. Hesp, I. Torre, D. Rodan-Legrain, P. Novelli, Y. Cao, S. Carr, S. Fang, P. Stepanov, D. Barcons-Ruiz, H. Herzig Sheinfux, K. Watanabe, T. Taniguchi, D. K. Efetov, E. Kaxiras, P. Jarillo-Herrero, M. Polini, and F. H. Koppens, Observation of interband collective excitations in twisted bilayer graphene, *Nature Physics* 2021 17:10 **17**, 1162 (2021).
- [22] R. Hillenbrand, T. Taubner, and F. Keilmann, Phonon-enhanced light matter interaction at the nanometre scale, *Nature* **418**, 159 (2002).
- [23] J. D. Caldwell, O. J. Glembocki, Y. Francescato, N. Sharac, V. Giannini, F. J. Bezares, J. P. Long, J. C. Owrutsky, I. Vurgaftman, J. G. Tischler, V. D. Wheeler, N. D. Bassim, L. M. Shirey, R. Kasica, and S. A. Maier, Low-loss, extreme subdiffraction photon confinement via silicon carbide localized surface phonon polariton resonators, *Nano letters* **13**, 3690 (2013).
- [24] C. Weisbuch, M. Nishioka, A. Ishikawa, and Y. Arakawa, Observation of the coupled exciton-photon mode splitting in a semiconductor quantum microcavity, *Physical Review Letters* **69**, 3314 (1992).
- [25] A. Kavokin, Exciton-polaritons in microcavities: Recent discoveries and perspectives, *physica status solidi (b)* **247**, 1898 (2010).
- [26] H. Deng, H. Haug, and Y. Yamamoto, Exciton-polariton Bose-Einstein condensation, *Reviews of Modern Physics* **82**, 1489 (2010).
- [27] V. Timofeev and D. Sanvitto, *Exciton polaritons in microcavities : new frontiers* (Springer, 2012) p. 401.
- [28] Y. Yamamoto and A. Imamoglu, *Mesoscopic Quantum Optics* (John Wiley, 1999) p. 320.
- [29] X. Liu, T. Galfsky, Z. Sun, F. Xia, E.-c. Lin, Y.-H. Lee, S. Kéna-Cohen, and V. M. Menon, Strong light-matter coupling in two-dimensional atomic crystals, *Nature Photonics* **9**, 30 (2014).
- [30] L. Novotny, Strong coupling, energy splitting, and level crossings: A classical perspective, *American Journal of Physics* **78**, 1199 (2010).
- [31] T. Byrnes, N. Y. Kim, and Y. Yamamoto, Exciton-polariton condensates, *Nature Physics* 2014 10:11 **10**, 803 (2014).
- [32] P. Alonso-González, A. Y. Nikitin, Y. Gao, A. Woessner, M. B. Lundeberg, A. Principi, N. Forcellini, W. Yan, S. Vélez, A. J. Huber, K. Watanabe, T. Taniguchi, F. Casanova, L. E. Hueso, M. Polini, J. Hone, F. H. L. Koppens, and R. Hillenbrand, Acoustic terahertz graphene plasmons revealed by photocurrent nanoscopy, *Nature Nanotechnology* 2016 12:1 **12**, 31 (2016).
- [33] P. Alonso-González, A. Y. Nikitin, F. Golmar, A. Centeno, A. Pesquera, S. Vélez, J. Chen, G. Navickaite, F. Koppens, A. Zurutuza, F. Casanova, L. E. Hueso, and R. Hillenbrand, Controlling graphene plasmons with resonant metal antennas and spatial conductivity patterns, *Science* **344**, 1369 (2014).
- [34] L. Ju, B. Geng, J. Horng, C. Girit, M. Martin, Z. Hao, H. A. Bechtel, X. Liang, A. Zettl, Y. R. Shen, and F. Wang, Graphene plasmonics for tunable terahertz metamaterials, *Nature Nanotechnology* 2011 6:10 **6**, 630 (2011).
- [35] G. X. Ni, A. S. McLeod, Z. Sun, L. Wang, L. Xiong, K. W. Post, S. S. Sunku, B. Y. Jiang, J. Hone, C. R. Dean, M. M. Fogler, and D. N. Basov, Fundamental limits to graphene plasmonics, *Nature* 2018 557:7706 **557**, 530 (2018).
- [36] Z. Sun, J. Gu, A. Ghazaryan, Z. Shotan, C. R. Conside, M. Dollar, B. Chakraborty, X. Liu, P. Ghaemi, S. Kéna-Cohen, and V. M. Menon, Optical control of room-temperature valley polaritons, *Nature Photonics* 2017 11:8 **11**, 491 (2017).
- [37] I. Epstein, B. Terrés, A. J. Chaves, V. V. Pusapati, D. A. Rhodes, B. Frank, V. Zimmermann, Y. Qin, K. Watanabe, T. Taniguchi, H. Giessen, S. Tongay, J. C. Hone, N. M. Peres, and F. H. Koppens, Near-unity light absorption in a monolayer ws_2 van der Waals heterostructure cavity, *Nano Letters* **20**, 3545 (2020).
- [38] J. Horng, E. W. Martin, Y. H. Chou, E. Courtade, T. C. Chang, C. Y. Hsu, M. H. Wentzel, H. G. Ruth, T. C. Lu, S. T. Cundiff, F. Wang, and H. Deng, Perfect absorption by an atomically thin crystal, *Physical Review Applied* **14**, 024009 (2020).
- [39] H. H. Fang, B. Han, C. Robert, M. A. Semina, D. Lagarde, E. Courtade, T. Taniguchi, K. Watanabe, T. Amand, B. Urbaszek, M. M. Glazov, and X. Marie, Control of the Exciton Radiative Lifetime in van der Waals Heterostructures, *Physical Review Letters* **123**, 067401 (2019).
- [40] J. Horng, Y.-H. Chou, Y.-H. Chou, T.-C. Chang, C.-Y. Hsu, T.-C. Lu, H. Deng, and H. Deng, Engineering radiative coupling of excitons in 2D semiconductors, *Optica*, Vol. 6, Issue 11, pp. 1443-1448 **6**, 1443 (2019).
- [41] J. C. Henriques, I. Epstein, and N. M. Peres, Absorption and optical selection rules of tunable excitons in biased bilayer graphene, *Physical Review B* **105**, 045411 (2022).
- [42] M. F. Quintela and N. M. Peres, Tunable excitons in rhombohedral trilayer graphene, *Physical Review B* **105**, 205417 (2022).

- [43] L. Ju, L. Wang, T. Cao, T. Taniguchi, K. Watanabe, S. G. Louie, F. Rana, J. Park, J. Hone, F. Wang, and P. L. McEuen, Tunable excitons in bilayer graphene, *Science* **358**, 907 (2017).
- [44] C. H. Park and S. G. Louie, Tunable excitons in biased bilayer graphene, *Nano Letters* **10**, 426 (2010).
- [45] L. Ju, L. Wang, X. Li, S. Moon, M. Ozerov, Z. Lu, T. Taniguchi, K. Watanabe, E. Mueller, F. Zhang, D. Smirnov, F. Rana, and P. L. McEuen, Unconventional valley-dependent optical selection rules and Landau level mixing in bilayer graphene, *Nature Communications* 2020 11:1 **11**, 1 (2020).
- [46] V. G. Duarte, D. R. Da Costa, N. M. Peres, L. K. Teles, and A. J. Chaves, Moiré excitons in biased twisted bilayer graphene under pressure, *Physical Review B* **110**, 035405 (2024).
- [47] E. V. Castro, K. S. Novoselov, S. V. Morozov, N. M. Peres, J. M. Dos Santos, J. Nilsson, F. Guinea, A. K. Geim, and A. H. Neto, Biased bilayer graphene: Semiconductor with a gap tunable by the electric field effect, *Physical Review Letters* **99**, 216802 (2007).
- [48] Y. Zhang, T. T. Tang, C. Girit, Z. Hao, M. C. Martin, A. Zettl, M. F. Crommie, Y. R. Shen, and F. Wang, Direct observation of a widely tunable bandgap in bilayer graphene., *Nature* **459**, 820 (2009).
- [49] J. B. Oostinga, H. B. Heersche, X. Liu, A. F. Morpurgo, and L. M. Vandersypen, Gate-induced insulating state in bilayer graphene devices, *Nature Materials* 2007 7:2 **7**, 151 (2007).
- [50] G. Wang, A. Chernikov, M. M. Glazov, T. F. Heinz, X. Marie, T. Amand, and B. Urbaszek, Colloquium: Excitons in atomically thin transition metal dichalcogenides, *Reviews of Modern Physics* **90**, 021001 (2018).
- [51] T. G. Pedersen, Intraband effects in excitonic second-harmonic generation, *Physical Review B - Condensed Matter and Materials Physics* **79**, 235432 (2009).
- [52] C. Aversa and J. E. Sipe, Nonlinear optical susceptibilities of semiconductors: Results with a length-gauge analysis, *Physical Review B* **52**, 14636 (1995).
- [53] E-Periodica - On the Definition of the Renormalization Constant in Quantum Electrodynamics, *Physical Review B* **109**, 121408 (2024).
- [54] H. Lehmann, Über Eigenschaften von Ausbreitungsfunktionen und Renormierungskonstanten quantisierter Felder, *Il Nuovo Cimento* **11**, 342 (1954).
- [55] M. F. C. M. Quintela, N. M. R. Peres, and T. G. Pedersen, Tunable nonlinear excitonic optical response in biased bilayer graphene, *Physical Review B* **110**, 085433 (2024).
- [56] I. Epstein, A. J. Chaves, D. A. Rhodes, B. Frank, K. Watanabe, T. Taniguchi, H. Giessen, J. C. Hone, N. M. R. Peres, and F. H. L. Koppens, Highly confined in-plane propagating exciton-polaritons on monolayer semiconductors, *2D Materials* **7**, 035031 (2020).
- [57] T. Eini, T. Asherov, Y. Mazor, and I. Epstein, Valley-polarized hyperbolic exciton polaritons in few-layer two-dimensional semiconductors at visible frequencies, *Physical Review B* **106**, L201405 (2022).
- [58] P. Li, M. Lewin, A. V. Kretinin, J. D. Caldwell, K. S. Novoselov, T. Taniguchi, K. Watanabe, F. Gaussmann, and T. Taubner, Hyperbolic phonon-polaritons in boron nitride for near-field optical imaging and focusing, *Nature Communications* 2015 6:1 **6**, 1 (2015).
- [59] I. Kats, T. Eini, and I. Epstein, 2D Semiconductors Superlattices as Hyperbolic Materials, arXiv:2411.14785 (2024).
- [60] A. Woessner, M. B. Lundberg, Y. Gao, A. Principi, P. Alonso-González, M. Carrega, K. Watanabe, T. Taniguchi, G. Vignale, M. Polini, J. Hone, R. Hillenbrand, and F. H. L. Koppens, Highly confined low-loss plasmons in graphene-boron nitride heterostructures, *Nature Materials* 2014 14:4 **14**, 421 (2014).
- [61] M. B. Lundberg, Y. Gao, R. Asgari, C. Tan, B. V. Duppen, M. Autore, P. Alonso-González, A. Woessner, K. Watanabe, T. Taniguchi, R. Hillenbrand, J. Hone, M. Polini, and F. H. Koppens, Tuning quantum nonlocal effects in graphene plasmonics, *Science* **357**, 187 (2017).
- [62] D. A. Iranzo, S. Nanot, E. J. Dias, I. Epstein, C. Peng, D. K. Efetov, M. B. Lundberg, R. Parret, J. Osmond, J. Y. Hong, J. Kong, D. R. Englund, N. M. Peres, and F. H. Koppens, Probing the ultimate plasmon confinement limits with a van der Waals heterostructure, *Science* **360**, 291 (2018).
- [63] I. Epstein, D. Alcaraz, Z. Huang, V. V. Pusapati, J. P. Hugonin, A. Kumar, X. M. Deputy, T. Khodkov, T. G. Rappoport, J. Y. Hong, N. M. Peres, J. Kong, D. R. Smith, and F. H. Koppens, Far-field excitation of single graphene plasmon cavities with ultracompressed mode volumes, *Science* **368**, 1219 (2020).
- [64] S. G. Menabde, I. H. Lee, S. Lee, H. Ha, J. T. Heiden, D. Yoo, T. T. Kim, T. Low, Y. H. Lee, S. H. Oh, and M. S. Jang, Real-space imaging of acoustic plasmons in large-area graphene grown by chemical vapor deposition, *Nature Communications* 2021 12:1 **12**, 1 (2021).
- [65] F. Stern, Polarizability of a Two-Dimensional Electron Gas, *Physical Review Letters* **18**, 546 (1967).
- [66] G. S. Agarwal, D. N. Pattanayak, and E. Wolf, Electromagnetic fields in spatially dispersive media, *Physical Review B* **10**, 1447 (1974).
- [67] S. Y. Lee, J. H. Park, and D. G. Thomas, Theoretical and Experimental Effects of Spatial Dispersion on the Optical Properties of Crystals, *Physical Review* **132**, 563 (1963).
- [68] S. Y. Lee, J. H. Park, and D. G. Thomas, In-plane exciton polaritons versus plasmon polaritons: Nonlocal corrections, confinement, and loss, *Physical Review B* **109**, 10.1103/PHYSREVB.109.L121408 (2024).
- [69] L. Wang, I. Meric, P. Y. Huang, Q. Gao, Y. Gao, H. Tran, T. Taniguchi, K. Watanabe, L. M. Campos, D. A. Muller, J. Guo, P. Kim, J. Hone, K. L. Shepard, and C. R. Dean, One-dimensional electrical contact to a two-dimensional material, *Science* **342**, 614 (2013).
- [70] A. Fali, S. T. White, T. G. Folland, M. He, N. A. Aghamiri, S. Liu, J. H. Edgar, J. D. Caldwell, R. F. Haglund, and Y. Abate, Refractive Index-Based Control of Hyperbolic Phonon-Polariton Propagation, *Nano Letters* **19**, 7725 (2019).
- [71] S. Dai, J. Quan, G. Hu, C. W. Qiu, T. H. Tao, X. Li, and A. Alù, Hyperbolic Phonon Polaritons in Suspended Hexagonal Boron Nitride, *Nano Letters* **19**, 1009 (2019).
- [72] G. Hu, J. Shen, C. W. Qiu, A. Alù, and S. Dai, Phonon Polaritons and Hyperbolic Response in van der Waals Materials, *Advanced Optical Materials* **8**, 1901393 (2020).
- [73] G. Ni, A. S. McLeod, Z. Sun, J. R. Matson, C. F. B. Lo, D. A. Rhodes, F. L. Ruta, S. L. Moore, R. A. Vitalone,

- R. Cusco, L. Artús, L. Xiong, C. R. Dean, J. C. Hone, A. J. Millis, M. M. Fogler, J. H. Edgar, J. D. Caldwell, and D. N. Basov, Long-Lived Phonon Polaritons in Hyperbolic Materials, *Nano Letters* **21**, 5767 (2021).
- [74] Z. Jacob, Hyperbolic phonon-polaritons, *Nature Materials* 2014 13:12 **13**, 1081 (2014).
- [75] A. J. Giles, S. Dai, O. J. Glembocki, A. V. Kretinin, Z. Sun, C. T. Ellis, J. G. Tischler, T. Taniguchi, K. Watanabe, M. M. Fogler, K. S. Novoselov, D. N. Basov, and J. D. Caldwell, Imaging of Anomalous Internal Reflections of Hyperbolic Phonon-Polaritons in Hexagonal Boron Nitride, *Nano Letters* **16**, 3858 (2016).
- [76] A. Poddubny, I. Iorsh, P. Belov, and Y. Kivshar, Hyperbolic metamaterials, *Nature Photonics* 2013 7:12 **7**, 948 (2013).
- [77] P. Shekhar, J. Atkinson, and Z. Jacob, Hyperbolic metamaterials: fundamentals and applications, *Nano Convergence* 2014 1:1 **1**, 1 (2014).
- [78] L. Ferrari, C. Wu, D. Lepage, X. Zhang, and Z. Liu, Hyperbolic metamaterials and their applications, *Progress in Quantum Electronics* **40**, 1 (2015).
- [79] O. L. Berman, R. Y. Kezerashvili, and K. Ziegler, Superfluidity and collective properties of excitonic polaritons in gapped graphene in a microcavity, *PHYSICAL REVIEW B* **86**, 235404 (2012).
- [80] S. De Liberato, Perspectives for gapped bilayer graphene polaritonics, *PHYSICAL REVIEW B* **92**, 125433 (2015).
- [81] J. C. Henriques, N. A. Mortensen, and N. M. Peres, Analytical description of the 1s exciton linewidth temperature dependence in transition metal dichalcogenides, *Physical Review B* **103**, 235402 (2021).
- [82] E. McCann, D. S. Abergel, and V. I. Fal'ko, Electrons in bilayer graphene, *Solid State Communications* **143**, 110 (2007).
- [83] J. Yan, E. A. Henriksen, P. Kim, and A. Pinczuk, Observation of anomalous phonon softening in bilayer graphene, *Physical Review Letters* **101**, 136804 (2008).
- [84] C. H. Park, F. Giustino, M. L. Cohen, and S. G. Louie, Electron-phonon interactions in graphene, bilayer graphene, and graphite, *Nano Letters* **8**, 4229 (2008).
- [85] J. H. Chen, C. Jang, S. Xiao, M. Ishigami, and M. S. Fuhrer, Intrinsic and extrinsic performance limits of graphene devices on SiO₂, *Nature nanotechnology* **3**, 206 (2008).
- [86] K. M. Borysenko, J. T. Mullen, X. Li, Y. G. Semenov, J. M. Zavada, M. B. Nardelli, and K. W. Kim, Electron-Phonon Interactions in Bilayer Graphene: A First Principles Approach, arXiv (2010).
- [87] Y. E. Lozovik, S. L. Ogarkov, and A. A. Sokolik, Electron-electron and electron-hole pairing in graphene structures, *Philosophical Transactions of the Royal Society A: Mathematical, Physical and Engineering Sciences* **371**, 20120177 (2013).
- [88] X. Li, K. M. Borysenko, M. B. Nardelli, and K. W. Kim, Electron transport properties of bilayer graphene, *Physical Review B - Condensed Matter and Materials Physics* **84**, 115411 (2011).
- [89] K. Zou, X. Hong, and J. Zhu, Effective mass of electrons and holes in bilayer graphene: Electron-hole asymmetry and electron-electron interaction, *Physical Review B - Condensed Matter and Materials Physics* **84**, 115412 (2011).
- [90] J. Yan, M. H. Kim, J. A. Elle, A. B. Sushkov, G. S. Jenkins, H. M. Milchberg, M. S. Fuhrer, and H. D. Drew, Dual-gated bilayer graphene hot-electron bolometer, *Nature nanotechnology* **7**, 472 (2012).
- [91] Z. J. Estrada, B. Dellabetta, U. Ravaioli, and M. J. Gilbert, Phonon-limited transport in graphene pseudospintronic devices, *IEEE Electron Device Letters* **33**, 1465 (2012).
- [92] P. T. Araujo, D. L. Mafra, K. Sato, R. Saito, J. Kong, and M. S. Dresselhaus, Unraveling the interlayer-related phonon self-energy renormalization in bilayer graphene, *Scientific Reports* 2012 2:1 **2**, 1 (2012).
- [93] J. Xi, M. Long, L. Tang, D. Wang, and Z. Shuai, First-principles prediction of charge mobility in carbon and organic nanomaterials, *Nanoscale* **4**, 4348 (2012).
- [94] J. Li, L. Z. Tan, K. Zou, A. A. Stabile, D. J. Seiwell, K. Watanabe, T. Taniguchi, S. G. Louie, and J. Zhu, Effective mass in bilayer graphene at low carrier densities: The role of potential disorder and electron-electron interaction, *Physical Review B* **94**, 161406 (2016).
- [95] Y. Ge and T. S. Fisher, Photoconductivity calculations of bilayer graphene from first principles and deformation-potential approach, *Physical Review B* **101**, 235429 (2020).
- [96] E. L. Silva, M. C. Santos, J. M. Skelton, T. Yang, T. Santos, S. C. Parker, and A. Walsh, Electronic and Phonon Instabilities in Bilayer Graphene under Applied External Bias, *Materials Today: Proceedings* **20**, 373 (2020).
- [97] W. Lin and P. Zhuang, Holes distribution in bilayer graphene, *Applied Surface Science* **595**, 153517 (2022).
- [98] Y. Z. Chou, F. Wu, J. D. Sau, and S. Das Sarma, Acoustic-phonon-mediated superconductivity in Bernal bilayer graphene, *Physical Review B* **105**, L100503 (2022).
- [99] field-and-wave-electromagnetics-david-k-cheng : David k Cheng : F
- [100] P. A. D. Gonçalves and N. M. R. Peres, An Introduction to Graphene Plasmonics, *An Introduction to Graphene Plasmonics*, 1 (2016).